Ocean Dynamics (2024) 74:967–986
https://doi.org/10.1007/s10236-024-01644-5

Enhanced eddy activity along the Subantarctic Front under intensified westerly winds

Takuro Matsuta[1] · Humio Mitsudera[2] · Yukio Masumoto[3,4] · Hideharu Sasaki[4] · Ryo Furue[4] · Tomomichi Ogata[4]

Received: 8 July 2024 / Accepted: 9 October 2024 / Published online: 24 October 2024

Abstract
The westerlies in the southern hemisphere have intensified and shifted southward since the middle of the twentieth century. Previous studies have indicated that the expected increase in isopycnal slopes and acceleration of the Antarctic Circumpolar Current (ACC) is considerably weakened by the strengthening of mesoscale eddies and that this "eddy saturation" occurs mainly downstream of the major bottom topographic features such as the Kerguelen Plateau. Such eddy "hotspots" are thus considered to regulate the ACC responses to changes in external forcing. To improve our understanding of the ACC response to intensified winds, a sensitivity study is conducted using an eddy-resolving quasi-global ocean general circulation model named "OFES." The reference run is driven by a climatological atmospheric forcing and the sensitivity run is driven by artificially intensified climatological westerlies. Our new finding is that the baroclinic energy pathway is enhanced over the Subantarctic Front (SAF) as well as over the hotspots identified by previous studies. A linear stability analysis indicates that the spin-up of the subtropical gyres north of the SAF and the enhanced Ekman upwelling south of the SAF by the intensified wind stress curl increase the vertical shear of zonal velocity along the SAF, enhancing baroclinic instability. We have also performed the same stability analysis comparing the 1985–2018 and 1955–1984 periods of a hindcast run of OFES, confirming the result from the climatological sensitivity study. These results suggest that the SAF is another eddy hotspot when the wind stress curl keeps increasing.

Keywords Antarctic Circumpolar Current · Lorenz energy cycle · Eddy-mean flow interactions · Baroclinic instability

1 Introduction

The Antarctic Circumpolar Current (ACC) circulates over the globe through the Drake Passage (56˚S-59˚S) and connects three major ocean sectors directly. Because of this unblocked structure, the ACC transport is responsible for the tracer transports in the ocean circulation (Talley 2013; Rintoul 2018). A critical feature of ACC is its vigorous eddy field (Rintoul 2018). Strong westerly winds drive the northward Ekman transport, with downwelling north of the Subantarctic Front (SAF) and upwelling south of it. Therefore, the isopycnal surface tilts upward to the south, sustaining the strong zonal geostrophic current of ACC. If the intensified westerly becomes sufficiently strong, the baroclinic instability generates vigorous transient eddies. Previous studies have suggested that the eddy dynamics determines the responses of ACC's circumpolar transport to changes in atmospheric forcing. In particular, a concept sometimes called "eddy saturation" (Gnanadesikan and Hallberg 2000) has been focused on in recent studies as a mechanism of ACC responses to changes in westerly winds. As stronger westerlies tend to steepen the local isopycnal slope, a stronger eddy field is generated. Theoretical considerations point out that the increased eddy momentum transport toward the ocean bottom leads to slight changes in the thermal wind transport in the upper layer (Marshall and Speer 2012; Rintoul 2018; Thompson and Naveira Garabato 2014; Straub 1993; Gnanadesikan and Hallberg 2000; Abernathey and Cessi 2014), whereas the large-scale

✉ Takuro Matsuta
matsuta@ees.hokudai.ac.jp

[1] Faculty of Environmental Earth Science, Hokkaido University, Sapporo, Japan

[2] Pan-Okhotsk Research Center, Institute of Low Temperature Science, Hokkaido University, Sapporo, Japan

[3] Department of Earth and Planetary Science, Graduate School of Science, The University of Tokyo, Tokyo, Japan

[4] Application Laboratory, Japan Agency for Marine-Earth Science and Technology, Yokohama, Japan

linear momentum balance (Wang and Huang 1995; LaCasce and Isachsen 2010; Krupitsky and Cane 1994) as well as the low-resolution models (Fyfe and Saenko 2005, 2006; Saenko et al. 2005) predict a linear response to westerlies. Observations (Böning et al. 2008) as well as high-resolution models (Spence et al. 2010; Hallberg and Gnanadesikan 2006; Farneti et al. 2010; Dufour et al. 2012; Bishop et al. 2016; Zika et al. 2013) have shown much smaller changes in zonally and temporary averaged isopycnal slope than the linear theory and low-resolution models predicted in spite of increasing westerlies, supporting the eddy saturation concept.

Eddy activity is known to be localized downstream of where the ACC interacts with significant topographic features such as the Kerguelen Plateau (Fig. 1a) (Thompson and Sallée 2012; Thompson and Naveira Garabato 2014; Abernathey and Cessi 2014; Frenger et al. 2015; Foppert et al. 2017; Katsumata 2017; Barthel et al. 2017; Stewart and Hogg 2017; Foppert 2019; Jouanno and Capet 2020; Yung et al. 2022; Barthel et al. 2022; Stewart et al. 2023; Zhang et al. 2023; Matsuta and Masumoto 2023). Figure 1b shows the horizontal distribution of transient eddy kinetic energy (EKE) (defined in Section 2.2) averaged over 1993–2018 calculated from the Ssalto/Duacs satellite sea surface height product (delayed-time, Level 4; Copernicus Marine and Environment Monitoring Service, http://www.marine.copernicus.eu). Following Kim and Orsi (2014), we define a "southern ACC Front (SACCF)" as the −98.5-cm contour line of the time-averaged absolute dynamic topography and the SAF as the −3.5-cm line. Furthermore, we define an "ACC region" as the area between these two fronts. Within the ACC region, EKE values greater than 40 J m^{-3} are confined in the five dashed green boxes of Fig. 1b. We denote these regions as "hotspots" of transient eddies. In these hotspots, stationary Rossby waves are trapped by the mean flow (Hughes 2005), increasing the local density gradients and thereby enhancing baroclinic instability (Bischoff and Thompson 2014; Thompson and Naveira Garabato 2014; Chapman et al. 2015), whereas eddy activity is suppressed away from the topographic features (Abernathey and Cessi 2014; Thompson and Naveira Garabato 2014; Bischoff and Thompson 2014; Wu et al. 2017; Matsuta and Masumoto 2023).

Although many studies have focused on hotspots, little attention has been given to eddy responses along the SAF. In high-resolution numerical models under intensified westerlies in previous studies (Dufour et al. 2012; Bishop et al. 2016; Wu et al. 2017), EKE increased not only in the hotspots but also along the SAF; however, the authors did not discuss this point. In this paper, we revisit the enhancement of eddies under intensified westerlies in the Southern Ocean. We conduct a sensitivity experiment using an eddy-resolving ocean general circulation model (OGCM) called "OFES" (Masumoto et al. 2004; Sasaki et al. 2004; see Section 2). The reference run is driven by a climatological atmospheric forcing, and the sensitivity run is driven by artificially intensified climatological

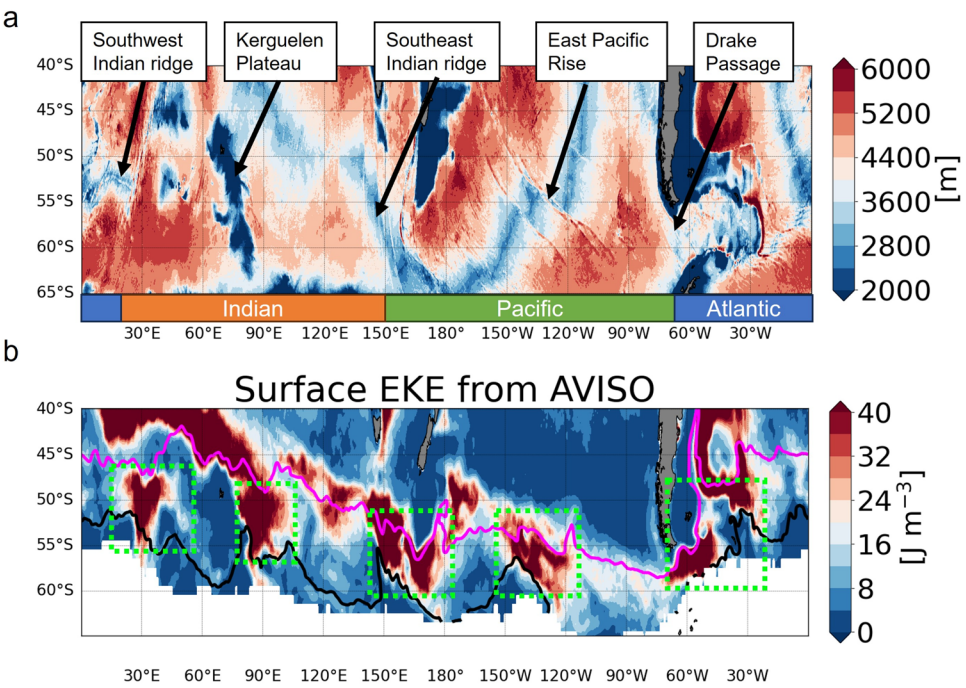

Fig. 1 **a** Ocean floor depth used in OFES. Major ridges associated with the eddy hotspots are indicated by black arrows. Orange, green, and blue colored boxes below the map indicate the zonal extents of the Indian, Pacific, and Atlantic sectors. **b** Surface EKE obtained from AVISO satellite altimetry observation. The magenta curve indicates the SAF and the black curve represents the Southern ACC Front. See the main text for the definitions of these fronts. Dashed green boxes roughly indicate the eddy hotspots

westerlies. We construct Lorenz energy diagrams and perform a two-layer quasi-geostrophic linear stability analysis to compare eddy activity and baroclinic instability between the two runs. In addition, to confirm our results from this climatological sensitivity experiment, we also compare two periods from an OFES time series run (Sasaki et al. 2008).

This manuscript is organized as follows. Section 2 describes the OGCM and introduces the Lorenz energy cycle (LEC). Section 3 presents the climatological sensitivity experiments and the result of the linear instability analysis. In Section 4, we evaluate the OFES hindcast to confirm our conclusions from the climatological experiments. Finally, Section 5 summarizes the paper.

2 Model and methods

2.1 Model description

We use version 1 of an eddy-resolving OGCM, named "OGCM For the Earth Simulator or OFES" (OFES1) (Masumoto et al. 2004) in this study. The computational domain extends from 75°S to 75°N. The horizontal resolution is $0.1° \times 0.1°$, which is reasonably fine to reproduce realistic mesoscale eddy activity (Sasaki et al. 2004). There are 54 levels in the vertical, with grid spacing increasing from 5 m at the surface to 330 m at the maximum depth of 6065 m. The model topography is constructed from the 1/30° bathymetry dataset created by the Ocean Circulation and Climate Advanced Modeling Project (OCCAM) at the Southampton Oceanography Centre (obtained through NOAA/GFDL). OFES was confirmed to reasonably reproduce the stratifications and eddy activities in the Southern Ocean (Matsuta 2022).

OFES1 was initially spun-up for 70 years under monthly mean climatological wind stresses calculated from 1950 to 1999 period of the NCEP/NCAR reanalysis (Kalnay et al. 1996). We investigate the final 5 years as a reference run named "E1". The sensitivity run, "E2", is started from the 50th year of the spin-up and integrated for 20 years but its wind stress is artificially intensified in the ACC as follows: the zonal and meridional components of wind stress are multiplied by a factor of 2 at 50°S and linearly decay to 1 at 40° and 60°S (Fig. 2a). This change corresponds to the 60% increase in the zonal momentum input, which is greater than that predicted in realistic models (e.g., Fyfe and Saenko (2006)), but we use this configuration to obtain clear deterministic responses because eddy-resolving models inevitably generates intrinsic or chaotic variability (Hallberg and Gnanadesikan 2006; Treguier et al. 2010; Hogg et al. 2022) in addition to the deterministic dynamical response we explore. To confirm the realism of sensitivity experiment, we will compare it with the OFES hindcast in Section 4. The three-day averaged outputs of the final 5 years are analyzed for each run.

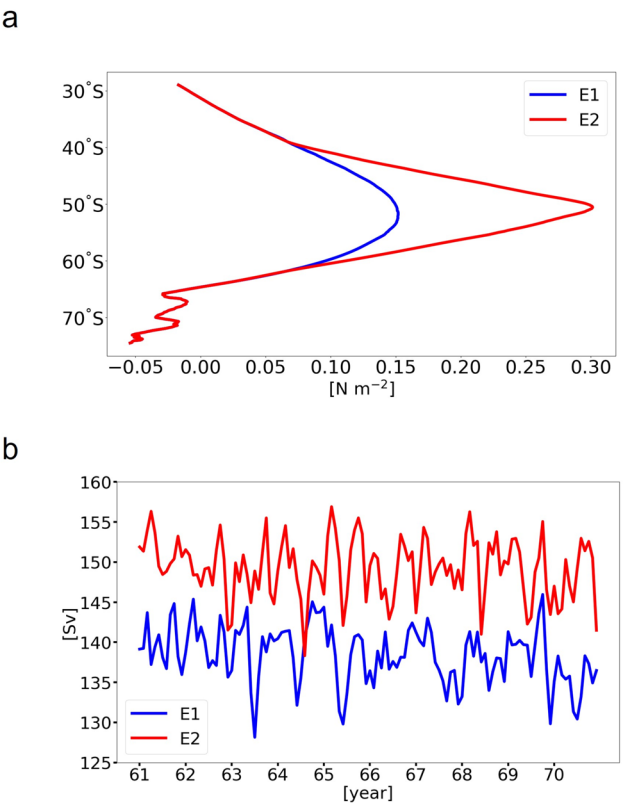

Fig. 2 **a** Zonally and annually averaged zonal wind stress for the E1 simulation (blue) and E2 simulation (red). **b** Monthly averaged transport across the Drake Passage for the E1 simulation (blue) and E2 simulation (red) for the period between the 61st and 70th year

To confirm that OFES reproduces the realistic circumpolar transport, the monthly mean zonal transport across the Drake Passage for the final 10 years is shown in Fig. 2b. The mean and standard deviation are 138 ± 13 Sv for the E1 run. The variability includes the seasonal variability due to the forcing and intrinsic variability (Hallberg and Gnanadesikan 2006). This transport is consistent with Koenig et al.'s (2014) estimate based on observations, 141 ± 2.7 Sv but smaller than Donohue et al.'s (2016) estimate, 173.3 ± 10.7 Sv. In the E2 run, the mean transport is 149 ± 3.7 Sv, which is only an 8.0% increase from the E1 run despite the 60% increase in wind stress, suggesting eddy saturation, i.e., a reduced sensitivity of circumpolar transport to wind stress.

2.2 Description of energy pathways among energy reservoirs

We describe eddy–mean flow interaction in this region using the classical four-box LEC (Lorenz 1955) comprising mean kinetic energy (K_M), mean available potential energy (P_M), eddy available potential energy (P_E), and the EKE (K_E). The classical LEC misses nonlocal eddy–mean flow interactions (Murakami 2011; Chen et al. 2014, 2016; Youngs et al. 2017; Matsuta and Masumoto 2021) and has quantitative ambiguity depending on the choice of the background density stratification (Scotti and White 2014; Zemskova et al. 2015; Aiki et al. 2016). These potential problems likely do not affect our conclusions: Matsuta and Masumoto (2023) showed that eddy–mean flow interaction is mostly local in the Southern Ocean, and as we shall see, our conclusions do not depend on values of background density field.

A variable A is decomposed into mean and transient-eddy components as

$$A = \overline{A} + A', \tag{1}$$

where the overline denotes temporal average over years $66-70$ and the prime denotes the deviation from the mean. Herein, we designate this temporal averaged value as "mean." With the separation between the mean flow and eddy, the mean kinetic energy and mean available potential energy are respectively defined as

$$K_M(\mathbf{r}) = \frac{1}{2}\rho_0\left(\overline{u}^2 + \overline{v}^2\right), \tag{2}$$

$$P_M(\mathbf{r}) = -\frac{1}{2}\frac{g}{\partial_z \sigma_{bg}(z)}\overline{\sigma^*}^2, \tag{3}$$

and the EKE and eddy available potential energy are defined as

$$K_E(\mathbf{r}) = \frac{1}{2}\rho_0\left(\overline{u'^2} + \overline{v'^2}\right), \tag{4}$$

$$P_E(\mathbf{r}) = -\frac{1}{2}\frac{g}{\partial_z \sigma_{bg}(z)}\overline{\sigma'^2}, \tag{5}$$

where $\mathbf{r} = (x, y, z)$ is the position, $\rho_0 = 1035$ kg m^{-3} is the reference density, and $\sigma_{bg}(z)$ is the horizontal average of the time-mean potential density over the Southern Ocean (south of 30°S in this study). The deviation of density from the reference state is defined as

$$\sigma^*(t, \mathbf{r}) = \sigma(t, \mathbf{r}) - \sigma_{bg}(z). \tag{6}$$

With this definition,

$$\sigma' = \sigma - \overline{\sigma} = \left(\sigma^* + \sigma_{bg}\right) - \overline{\sigma^* + \sigma_{bg}} = \sigma^* - \overline{\sigma^*}. \tag{7}$$

It is noted that because in-situ density is not conservative, the definition of available potential energy is based on potential density (Aiki and Richards 2008; Scotti and White 2014; Zemskova et al. 2015; Aiki et al. 2016; Zhu et al. 2018; Matsuta and Masumoto 2023). We use 2000 m as the reference depth of the potential density, σ. We have confirmed (not shown) that our results are unchanged qualitatively if we calculate the LEC using the potential density referenced to the sea surface, ρ_θ.

The mean and eddy energy equations for the LEC are

$$\begin{aligned}&\frac{\partial}{\partial t}K_M + \nabla\cdot\left(\overline{\mathbf{u}}K_M\right) + \rho_0\nabla\cdot\left(\overline{\overline{u}\overline{\mathbf{u}'}} + \overline{\overline{v}\overline{\mathbf{u}'}}\right) + \nabla\cdot\left(\overline{\mathbf{u}}\overline{p^*}\right)\\ &= -g\overline{\sigma^*}\overline{w} - \rho_0\left[-\overline{u'\mathbf{u}'}\cdot\nabla\overline{u} - \overline{v'\mathbf{u}'}\cdot\nabla\overline{v}\right] + X_{K_M},\end{aligned} \tag{8}$$

$$\begin{aligned}&\frac{\partial}{\partial t}K_E + \nabla\cdot\left(\overline{\mathbf{u}}K_E + \overline{\mathbf{u}'\tfrac{1}{2}\rho_0\left(u'^2+v'^2\right)}\right) + \nabla\cdot\left(\overline{\mathbf{u}'p'}\right)\\ &= -g\overline{\sigma'w'} + \rho_0\left[-\overline{u'\mathbf{u}'}\cdot\nabla\overline{u} - \overline{v'\mathbf{u}'}\cdot\nabla\overline{v}\right] + X_{K_E},\end{aligned} \tag{9}$$

$$\begin{aligned}&\frac{\partial}{\partial t}P_M + \overline{\mathbf{u}}_h\cdot\nabla_h\left(P_M\right) + \nabla_h\cdot\left(-\overline{\sigma'\mathbf{u}'_h}\frac{g}{\partial_z\sigma_{bg}(z)}\overline{\sigma^*}\right)\\ &= g\overline{\sigma^*}\overline{w} - \frac{g}{\partial_z\sigma_{bg}(z)}\overline{\sigma'\mathbf{u}'_h}\cdot\nabla_h\overline{\sigma^*} + X_{P_M},\end{aligned} \tag{10}$$

$$\begin{aligned}&\frac{\partial}{\partial t}P_E + \overline{\mathbf{u}_h}\cdot\nabla_h\left(P_E\right) + \overline{\mathbf{u}'_h\cdot\nabla_h\left(-\tfrac{1}{2}\frac{g}{\partial_z\sigma_{bg}(z)}\sigma'^2\right)}\\ &= g\overline{\sigma'w'} + \frac{g}{\partial_z\sigma_{bg}(z)}\overline{\sigma'\mathbf{u}'_h}\cdot\nabla_h\overline{\sigma^*} + X_{P_E},\end{aligned} \tag{11}$$

where p^* is the combined sea surface elevation and hydrostatic pressure fluctuations referenced to the background pressure field, $p^* = p - p_{ref}(z)$, $\mathbf{u} = (u, v, w)$ is the three-dimensional velocity, $\mathbf{u}_h$ is the two-dimensional component of $\mathbf{u}$, ∇ is the gradient operator, ∇_h is the two-dimensional component of ∇, and $X_\#$ represents diabatic source and sink terms including work by wind stress and surface buoyancy flux.

Equations (8) and (10) indicate that K_M and P_M exchange energy through the vertical mean density flux, $C(K_M, P_M)$:

$$C(K_M, P_M) = g\overline{\sigma^*}\overline{w}, \tag{12}$$

where positive values indicate energy conversion from K_M to P_M. In the Southern Ocean, $C(K_M, P_M)$ mainly originates from the Ekman upwelling (Aiki et al. 2011; Roquet et al. 2011; Matsuta and Masumoto 2023). The second terms on the right-hand sides of Eqs. (8) and (9) are identical except for their signs and denoted by

$$C(K_M, K_E) = \rho_0 \left[-\overline{u'\mathbf{u}'} \cdot \nabla \overline{u} - \overline{v'\mathbf{u}'} \cdot \nabla \overline{v} \right], \tag{13}$$

where positive values indicate that energy is converted from K_M to K_E, representing barotropic instability. Similarly, we denote the second terms of Eqs. (10) and (11) by

$$C(P_M, P_E) = \frac{g}{\partial_z \sigma_{bg}(z)} \overline{\sigma' \mathbf{u}'_h} \cdot \nabla_h \overline{\sigma^*}, \tag{14}$$

which is the baroclinic conversion rate, indicating, when positive, that eddies are extracting potential energy from the mean stratification. The first terms on the right-hand sides of Eqs. (9) and (11), i.e.,

$$C(P_E, K_E) = -g\overline{\sigma' w'} \tag{15}$$

is the vertical eddy density flux, indicating conversion from P_E to EKE. Typically, $C(P_M, P_E)$ and $C(P_E, K_E)$ form a baroclinic-conversion energy pathway (Wind input $\rightarrow K_M \rightarrow P_M \rightarrow P_E \rightarrow K_E$), and if this is the dominant pathway, a qualitative argument needs only one of $C(P_M, P_E)$ and $C(P_E, K_E)$. Therefore, we focus on $C(P_E, K_E)$ as a proxy to baroclinic conversion, as we find $C(P_M, P_E)$ values sensitive to the choice of background stratification (Matsuta and Masumoto 2023). We have confirmed (not shown) that using $C(P_M, P_E)$ does not change our qualitative conclusions. We will analyze changes in these conversion terms, Eqs. (13) and (15), under intensified westerlies in the next section.

2.3 Linear stability analysis

To investigate the mechanism of the baroclinic energy pathway, we perform linear stability analysis on the classical Phillips model (Pedlosky 1987; Vallis 2017), a simple two-layer quasi-geostrophic system. Although simple, this and similar frameworks have been successfully used to explain the eddy dynamics of the Southern Ocean (e.g., Abernathey and Cessi 2014; Nadeau and Ferrari 2015; Youngs et al. 2019; Stewart et al. 2023).

The potential vorticity (PV) equation for each layer is as follows:

$$\left(\frac{\partial}{\partial t} + u_j \frac{\partial}{\partial x} + v_j \frac{\partial}{\partial y} \right) q_j = 0, \; j = 1,2, \tag{16}$$

where u_j and v_j are the zonal and meridional velocities of the j-th layer. Here, the quasi-geostrophic PV q_j is defined by

$$q_1 = \nabla_h^2 \psi_1 + \beta y + F_1 (\psi_2 - \psi_1), \tag{17}$$

$$q_2 = \nabla_h^2 \psi_2 + \beta y + F_2 (\psi_1 - \psi_2), \tag{18}$$

where ψ_1 and ψ_2 are the stream functions of the first and second layers, β is the planetary vorticity gradient, which is assumed to be constant, and F_1 and F_2 are given as follows:

$$F_1 = \frac{1}{1+\delta} L_d^{-2}, \tag{19}$$

$$F_2 = \frac{\delta}{1+\delta} L_d^{-2}, \tag{20}$$

where $\delta = H_1/H_2$ is the ratio of the layer thickness and H_1 and H_2 are the mean thicknesses of the first and second layers, respectively. Here, the baroclinic deformation radius is defined as

$$L_d = \left(\frac{g'}{f_0^2} \frac{H_1 H_2}{H_1 + H_2} \right)^{\frac{1}{2}}, \tag{21}$$

where f_0 is the Coriolis parameter and g' is the reduced gravity acceleration. We next assume a zonal background flow:

$$\Psi_j = -U_j y, \tag{22}$$

where U_j is the j-th layer background zonal velocity, and we consider the deviation from the background flow:

$$\psi'_j = \psi_j - \Psi_j, \tag{23}$$

and linearize Eq. (16). Although the real SAF is tilted southward, we confirmed that our results were unchanged qualitatively if we included meridional velocity in the background flow (see Appendix).

For simplicity, we assume that ψ'_j is independent of y and zonally periodic, and seek solutions of the form

$$\psi'_j = \mathrm{Re}\, A_j e^{ik(x-ct)}, \; j = 1,2 \tag{24}$$

where $k > 0$ is the zonal wavenumber, c is the phase speed of the disturbance, Re indicates the real part of the complex number, and A_j is the complex amplitude. As described in Appendix, nontrivial solutions exist if and only if c satisfies the following condition:

$$\begin{aligned} &\left[(U_1 - c)(-k^2 - F_1) + (\beta + F_1 \Delta U) \right] \left[(U_2 - c)(-k^2 - F_2) + (\beta - F_2 \Delta U) \right] \\ &\quad - (U_1 - c)(U_2 - c) F_1 F_2 = 0, \end{aligned} \tag{25}$$

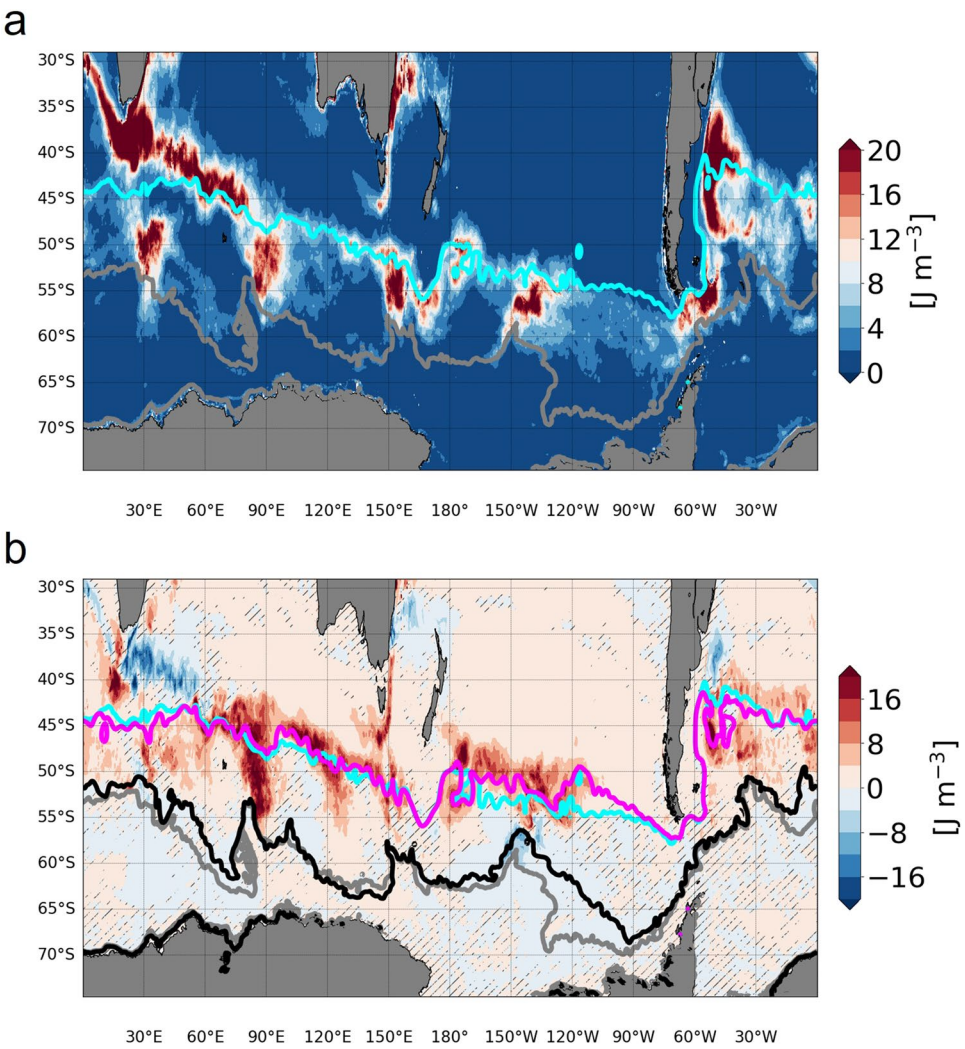

Fig. 3 **a** Vertically averaged EKE in the E1 simulation. The cyan curve represents the SAF as defined by the −30 cm sea surface elevation contour line and the gray curve represents SACCF as defined by the −160 cm sea surface elevation contour line, respectively. It is noted that the color scale is different from that of Fig. 1b. **b** Vertically averaged EKE anomaly of the E2 simulation from the E1 simulation. The magenta curve represents the SAF and the black curve represents SACCF in the E2 simulation. The cyan and gray curves are the same as those in the upper panel. The hatched regions indicate statistically nonsignificant anomaly values at a 95% confidence level in Welch's test. Welch's test is conducted for the monthly averaged time series during the final five years of each run

where $\Delta U = U_1 - U_2$ is the zonal velocity difference between the layers. We solve this equation for c as a function of k. Baroclinic instability occurs if and only if c has a positive imaginary part.

3 Results

3.1 Comparison of EKE

Figure 3 shows the horizontal distribution of the vertically averaged EKE in the E1 simulation. Here, We took the vertical average since the EKE of ACC has a vertical structure (Matsuta and Masumoto 2023) and thus the vertically averaged EKE reflects the energetics of the whole water column rather than the surface EKE. The reason why we show surface EKE in Fig. 1 is that the vertical structure is not available from observation. As before, the ACC region is defined as the region between the SAF and SACCF. For OFES, we use the −30- and −160-cm SSH contour lines to define the SAF and SACCF (Roquet et al. 2011). Within the ACC region, five hotspots are conspicuous, downstream of the prominent bottom topographic features around 30°E, 90°E, 160°E, 220°E, and 300°E, as shown by Matsuta and Masumoto (2023). There is also moderate eddy activity along the SAF.

The EKE anomaly of E2 from E1 is shown in Fig. 3b. As expected from previous research (Bishop et al. 2016; Wu et al. 2017), EKE is increased at the five hotspots. The anomalies exceed 10 J m^{-3} at the five hotspots and are statistically significant with a 95% confidence level in Welch's test, although they are relatively small in the Pacific and the Atlantic sector. In addition to the hotspots, EKE anomaly is large along the SAF in the Indian (50°E–130°E), Pacific (180°E–210°E), and Atlantic (330°E–360°E) sectors. This EKE increase along the SAF was observed in the plots in

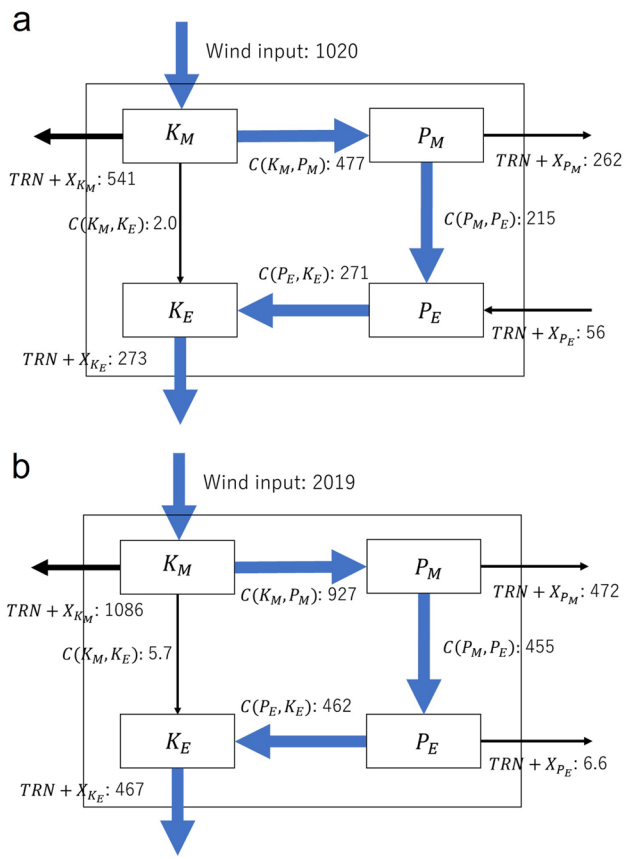

Fig. 4 LEC in GW (10^9 W) south of 40°S for (**a**) E1 and (**b**) E2. Arrows connecting boxes indicate energy conversion. Arrows pointing outside the box indicate an energy sink due to transport processes (*TRN*), which are composed of advection by mean and eddy flows, horizontal transport by pressure work, and interaction energy flux (Murakami 2011; Chen et al. 2014; Matsuta and Masumoto 2021, 2023). The diabatic source/sink including the surface force is represented by X. The baroclinic energy pathway (Wind input → K_M → P_M → P_E → K_E) is emphasized by thick blue arrows

previous studies (e.g. , Bishop et al. 2016; Wu et al. 2017), but the authors did not discuss the feature.

3.2 Energy pathway under intensified wind stress

To understand the EKE increase, the LEC is calculated for the E1 and E2 cases over the domain south of 40°S. In E1 (Fig. 4a), more than half (541 GW) of the wind energy input (1020 GW) to K_M is lost to dissipation. According to Aiki et al. (2011) and Roquet et al. (2011), a large part of this dissipation occurs within the Ekman layer. Almost all the remaining energy input (477 GW) is converted into P_E, which corresponds to the isopycnal steepening by the Ekman upwelling (see Matsuta and Masumoto (2023) for details). Approximately half of this amount is converted into K_E via the baroclinic energy pathway ($P_M \rightarrow P_E \rightarrow K_E$).

Under the intensified westerlies (Fig. 4b), the baroclinic energy pathway compensates for the increased energy input. The wind energy input of E2 is approximately twice as large as that of E1, and accordingly the baroclinic energy conversion route is twice as strong. This result is consistent with that of Wu et al. (2017). By contrast, the barotropic energy pathway ($K_M \rightarrow K_E$) is negligible in both runs: $C(K_M, K_E)$ is only ~1% of baroclinic energy conversion, $C(P_E, K_E)$.

To understand the baroclinic energy pathway, we next examine the horizontal distribution of baroclinic energy conversion, $C(P_E, K_E)$ (Fig. 5). In the E1 experiment, K_E generation by baroclinic instability (Fig. 5a) is large only in the hotspots and the downstream region of the Agulhas Return Current (ARC) (40°E – 80°E along the SAF). Under the intensified wind stress, $C(P_E, K_E)$ significantly increases over the SAF as well as at the hotspots (Fig. 5b), showing that the K_E enhancement along the SAF (Fig. 3b) can be attributed to baroclinic instability.

To quantify the contribution of the ACC region and SAF region to the baroclinic energy pathway changes, we calculate the cumulative integral of the $C(P_E, K_E)$ anomalies of E2 from E1 (Fig. 6). Here, the ACC region is defined as the region between the SAF and SACCF as before, and the SAF region is defined as a region within 3° north of the SAF. In ACC, the cumulative integral of $C(P_E, K_E)$ anomaly shows a jump from ~15 to ~40 GW at around 80°E, indicating that the baroclinic energy conversion downstream of Kerguelen Plateau is responsible for a large part of eddy responses inside the ACC. The region at around 120°E also has a substantial contribution. Indeed, the baroclinic energy conversion of this region becomes comparable with those of hotspots in E2 (see Fig. 5). In the SAF, by contrast, the value increases relatively uniformly in the regions between 50°E and 150°E and between 200°E and 250°E. A jump at the Drake Passage originates from the Brazil-Malvinas Confluence (Mason et al. 2017). The total anomaly integrated over the SAF (95 GW) is larger than that over the ACC (86 GW). Therefore, we conclude that the baroclinic energy pathway over the SAF is as important as that of the hotspots in the ACC interior under the intensified westerlies.

3.3 Baroclinic instability along the SAF

Figure 7a shows the SSH change from E1 to E2, which indicates that the subtropical gyres are intensified north of the SAF owing to the intensified wind-stress curl north of 50°S. South of 50°S, the sea level drops owing to the increased Ekman divergence. Fig. 7b shows the depth of potential density surface averaged zonally along the globe and its change from E1 to E2 (Hereafter, the potential density, ρ_θ, is referenced to the surface because we focus on the upper 2000 m.) Consistent with the intensified

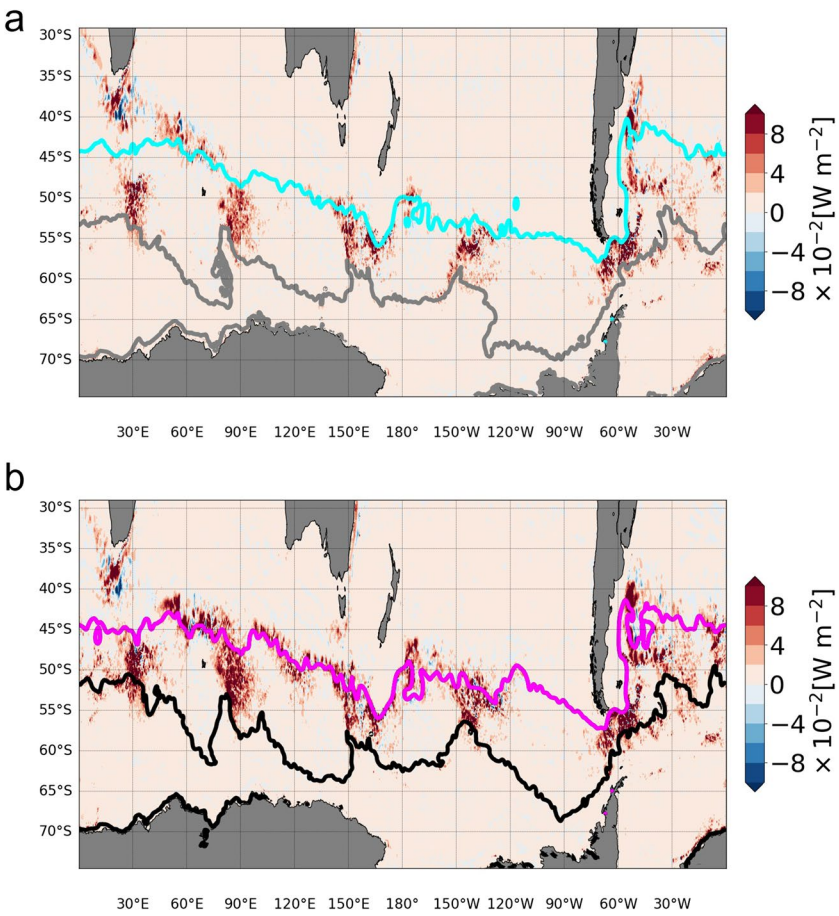

Fig. 5 Depth-integrated $C(P_E, K_E)$ for (**a**) E1 and (**b**) E2. The contours are the same as those in Fig. 3

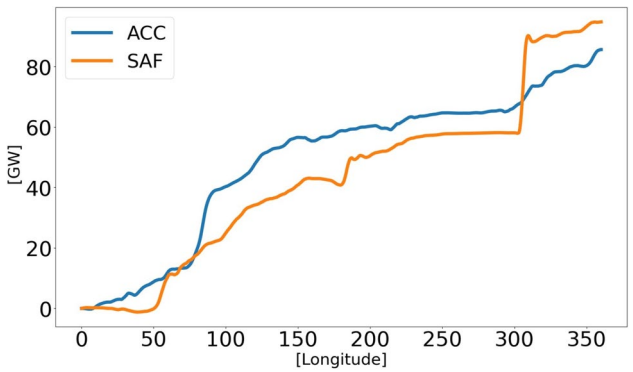

Fig. 6 Cumulative integral of the $C(P_E, K_E)$ anomaly integrated over the ACC (blue line) and SAF (orange line) regions. The integration is taken from 0.1°E. To reduce small-scale noises, each line is 2° moving-averaged

subtropical gyres, the thermocline depth increases by more than 120 m between $26.6\rho_\theta$ and $27.6\rho_\theta$ surfaces at around 45°S, while it shoals between $27.6\rho_\theta$ and $27.8\rho_\theta$ surfaces south of the SAF because of the intensified Ekman upwelling. Consequently, the isopycnal slope is steepened in the E2 case, increasing the vertical shear of zonal velocity (simply called *vertical shear* hereafter). It is noted that the local isopycnal steepening is not contradictory to the eddy saturation concept. According to Nadeau and Ferrari (2015), the circumpolar transport can be decomposed into a circumpolar component and a gyre component. The former component is responsible for the transport across the Drake Passage, while the latter does not have net circumpolar transport. Since the gyre component dominates in the SSH change (Fig. 7a), the local isopycnal steepening increases little circumpolar transport as seen in Fig. 2b.

We next look at the vertical shear and the buoyancy frequency, $\sqrt{-\frac{g}{\rho_0}\frac{\partial \rho_\theta}{\partial z}}$. These values are averaged over the SAF regions of the Indian sector (110°E–120°E, 45°S–48°S), Pacific sector (180°E–210°E, 49°S–52°S), Atlantic sector (330°E–360°E, 41°S–44°S), and ARC region (60°E–70°E, 44°S–46°S) (see green shaded boxes in Fig. 7a). The vertical shear increases over all the SAF regions in the upper 2000 m (Fig. 8). In particular, the shear becomes twice as large as that of E1 in the Indian sector and the ARC region at a depth of around 1000 m. As for the buoyancy frequency (Fig. 9), changes in the stratification appear small at the main pycnocline.

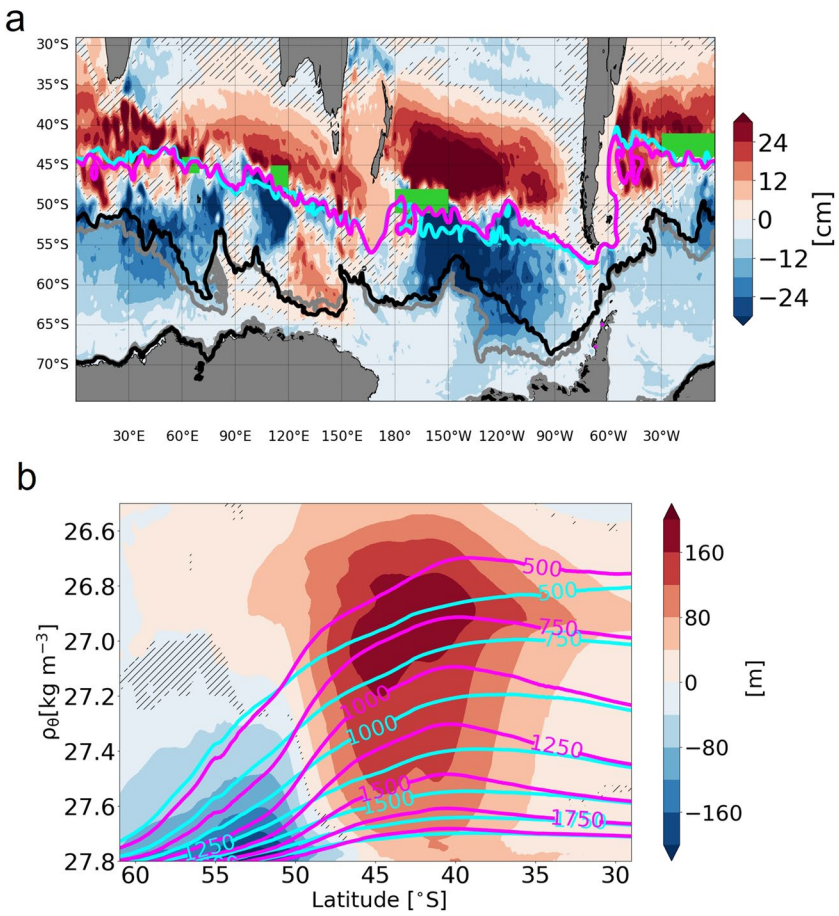

Fig. 7 **a** Sea-level change from E1 to E2. The curves are the same as those of Fig. 3. Green shaded boxes indicate the region where the vertical velocity shear and buoyancy frequency are calculated. **b** Zonally averaged density surface depth change from E1 to E2 in the potential density coordinate. The depth of density surface is calculated for every three-day mean data and averaged over time in the zonal direction. Potential density is referenced to the sea surface. Cyan and magenta contour lines denote the zonally averaged density surface depths for E1 and E2, respectively. In both plots, hatched regions indicate statistically nonsignificant values at a 95% confidence level in Welch's test. Welch's test is conducted for the monthly averaged time series during the final five years of each run

The results presented above suggest that the K_E increase along the SAF is probably due to enhanced baroclinic instability associated with the increased vertical shear. To test this hypothesis, we perform a linear stability analysis (see Section 2.3) of the SAF regions of the Indian sector (110°E–120°E, 45°S–48°S) as a representative case. We confirmed that the results of other SAF regions are similar to that of the Indian sector. To apply the two-layer model to OFES, we define the layer interface, i.e., the thermocline depth. We fit an exponential profile (Karsten et al. 2002; Youngs et al. 2019).

$$\rho_\theta^{(\mathrm{app})} = a \exp\left(\frac{z}{h_e}\right) + b \tag{26}$$

to the mean potential density profile from OFES and use h_e as the interface depth. Here, the mean potential density is defined as the temporal average over years $66-70$ in the depth-coordinate. The resultant interface depths are 1103 and 1278 m for E1 and E2, respectively, with the coefficient of determination, R^2 values of 0.94. The upper- and lower-layer background zonal velocities are defined to be the vertical averages of the mean velocity field within the layers, and the reduced gravity acceleration is defined with the mean potential density difference between the vertical averages within the layers. Table 1 summarizes the parameter values for the stability analysis for the Indian sector. Here, we assume that the total depth is 4000 m; however, these choices do not change our result qualitatively.

Using Eq. (25) (Section 2.2), we calculate the phase speed c for each k; the growth rate, $\mathrm{Re}(-ikc)$, is shown in Fig. 10a. Although baroclinic instability can occur in both E1 and E2 cases, the maximum growth rate E2 is more than twice as large in E2 as in E1: the most unstable mode in E2 has an e-folding timescale of 14 days, while that of E1 is 36 days. Moreover, the range of k where the baroclinic instability can occur is wider in E2. We also confirmed that if we exchange the parameters of E1 with those of E2 except for the upper-layer velocity, U_1, the growth rate shows little changes (Fig. 10b), indicating that the change in the growth rate between E1 and E2 is attributed to vertical shear. In summary, the intensified wind stress curl spins up the subtropical gyres north of the SAF, which deepens the thermocline, whereas the intensified upwelling south of the SAF shoals the thermocline. Consequently, the isopycnal slope increases across the SAF, increasing the vertical shear. The resultant increase in the growth rate of the baroclinic instability leads to the enhancement of the baroclinic energy pathway.

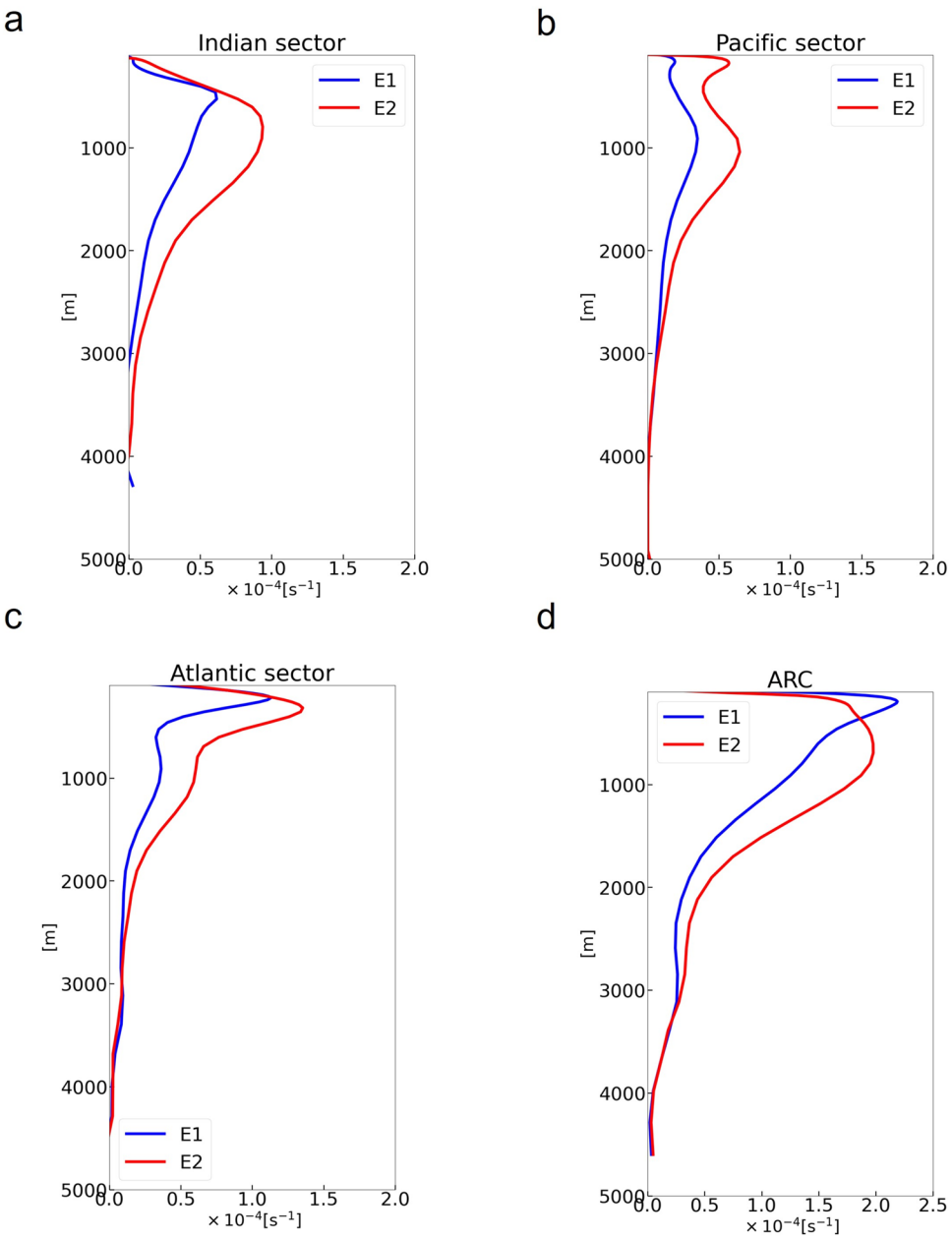

Fig. 8 Vertical profiles of the vertical shear of zonal velocity averaged over the SAF regions of the (**a**) Indian sector (110°E–120°E, 45°S–48°S), **b** Pacific sector (180°E–210°E, 49°S–52°S), **c** Atlantic sector (330°E–360°E, 41°S–44°S), and (**d**) Agulhas Return Current (60°E–70°E, 44°S–46°S). Blue and red lines correspond to the E1 and E2 cases, respectively

4 Discussion: comparison with the OFES hindcast

4.1 Description of the OFES hindcast

The result presented in the previous section is for an artificial change in wind stress (Fig. 2a). To assess the realism of the result, we analyze an OFES hindcast. Following the spin-up by climatological wind stress obtained from the NCEP-NCAR reanalysis (Kalnay et al. 1996) for 50 years, the hindcast run is forced by a daily mean atmosphere forcing based on NCEP-NCAR from 1950 to the present. Details of this hindcast are found in Sasaki et al. (2008). We use monthly mean outputs for the period from 1955 to 2018 because only monthly averages of each variable before 1987 are saved by the model owing to data storage constraints. Although the monthly data is sufficient for the stability analysis, EKE is underestimated because of the missing intra-monthly variabilities. However, the horizontal distribution of EKE is consistent with those obtained from three-day snapshots from 2000 to 2010 (Matsuta 2022; Matsuta and Masumoto 2023); therefore, the EKE values from monthly data can still be utilized as an index of mesoscale eddy activity.

As found in the past studies (Gong and Wang 1999; Marshall 2003; Fogt and Marshall 2020), the westerlies have been strengthening and shifting southward in the Southern Ocean

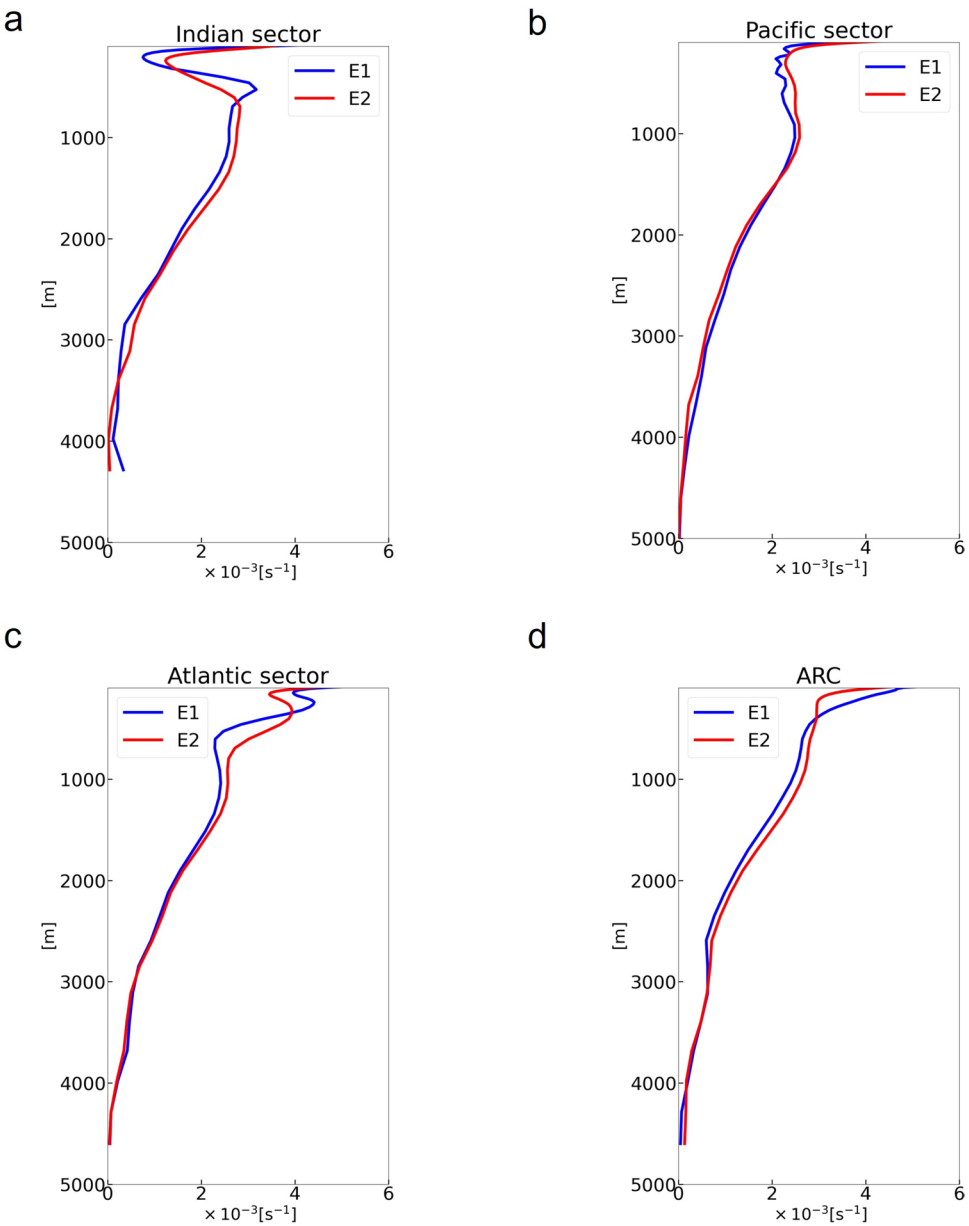

Fig. 9 Same as Fig. 8**a**-**d** but for the buoyancy frequency

Table 1 Parameter values used for the linear stability analysis. Dashes in the third column indicate that the values for E2 are the same as those for E1

	E1	E2
f_0	-1.1×10^{-4} s^{-1}	—
β	1.6×10^{-11} m^{-1}s^{-1}	—
U_1	6.7 cm s^{-1}	13.8 cm s^{-1}
U_2	0.47 cm s^{-1}	1.37 cm s^{-1}
H_1	1103 m	1278 m
H_2	2897 m	2722 m
g'	0.961×10^{-2} m s^{-2}	1.01×10^{-2} m s^{-2}

since the mid-twentieth century. The SAM index, which is a proxy for the meridional shift and magnitude of the westerlies, is defined as follows:

$$\mathrm{SAM} = SLP^*_{40°\mathrm{S}} - SLP^*_{65°\mathrm{S}}, \tag{27}$$

where $SLP^*_{40°\mathrm{S}}$ and $SLP^*_{65°\mathrm{S}}$ stand for normalized zonally averaged sea level pressure at 40˚S and 65˚S for every month, respectively (Gong and Wang 1999). In the present study, we obtain the sea level pressure from the NCEP/NCAR reanalysis. As shown in Fig. 11a, the SAM index has a positive trend, 0.38 per decade with a very small p-value. We divide the OFES hindcast into the 1955–1984 and 1985–2018 periods, calling them the weak-wind (WW)

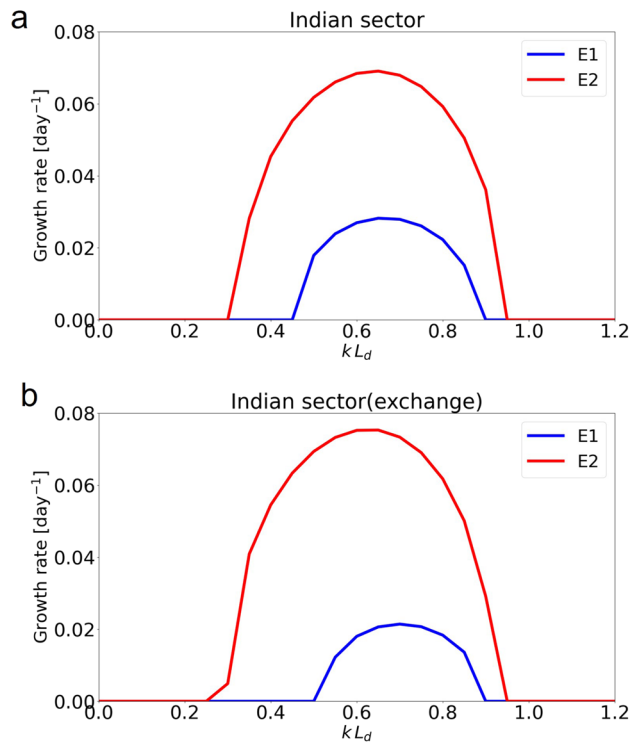

Fig. 10 **a** Blue and red lines indicate growth rate as a function of zonal wave number normalized by the deformation radius, L_d, for E1 and E2, respectively. **b** Same as (**a**), but the parameters of E1 are exchanged with those of E2 except for the upper-layer velocity

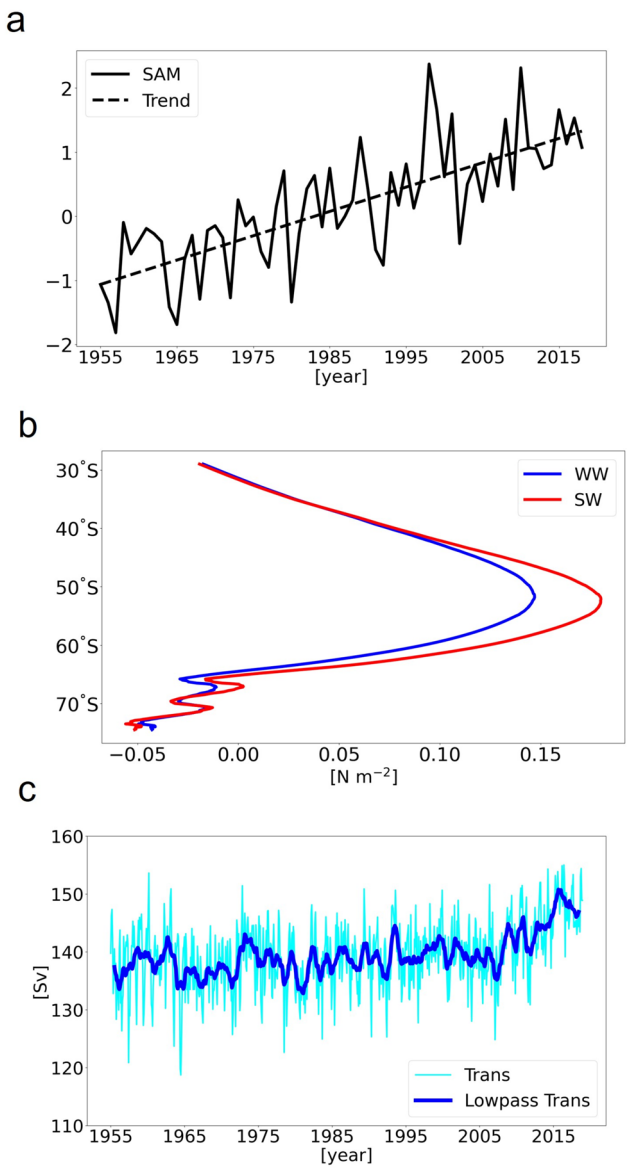

Fig. 11 **a** Time series of the annual averaged value of SAM index. Black dashed line indicates the linear trend (0.38 per decade with a very small p-value). **b** Zonally and annually averaged zonal wind stress for the WW (blue) and SW (red) periods. **c** Time series of the monthly transport across the Drake Passage (cyan curve) and the 13-month moving averaged one (blue curve)

and strong-wind (SW) periods, respectively. The WW and SW periods roughly fall in the negative and positive SAM periods, respectively. The zonally averaged zonal wind stress is shown in Fig. 11b. The zonal wind stress of the SW period is intensified between 40°S and 65°S compared to that of the WW period. The meridional distribution is roughly similar to that of the climatological experiment (c.f. Fig. 2a). The associated changes correspond to a 20% increase in the zonal momentum input to the analyzed region.

We show the volume transport across the Drake Passage from 1955 to 2018 (Fig. 11c). The mean circumpolar transport is 138 ± 5.5 Sv in the WW period, while the transport is 141 ± 5.6 Sv in the SW period, which are consistent with the observation of 141 ± 2.7 Sv by Koenig et al. (2014). The standard deviations during the two periods, 5.5 Sv and 5.6 Sv, are in the same order as the standard deviation of E1's (13 Sv) and E2's (2.7 Sv) circumpolar transport. The result shows that difference in the mean transport between the SW and WW periods is only 3 Sv, which is smaller than the transport increase that low-resolution models predict for the 20% intensification of the zonal wind stress over the ACC (Hallberg and Gnanadesikan 2006). This transport difference between the SW and WW periods decreases when the transport increase after 2010 is excluded. We thus consider the ACC of the OFES hindcast is in the eddy saturated regime.

Figure 12 presents plots of changes in wind stress curl and heat flux from the WW to the SW period. It is found that the wind stress curl anomaly is generally positive in the region between SAF and the latitude circle of 40°S, while it is generally negative in the southern half of the the ACC region (Fig. 12a). We confirmed that the anomaly between the two periods is significant at the 95% confidence level in Welch's test. These wind changes should strengthen the subtropical

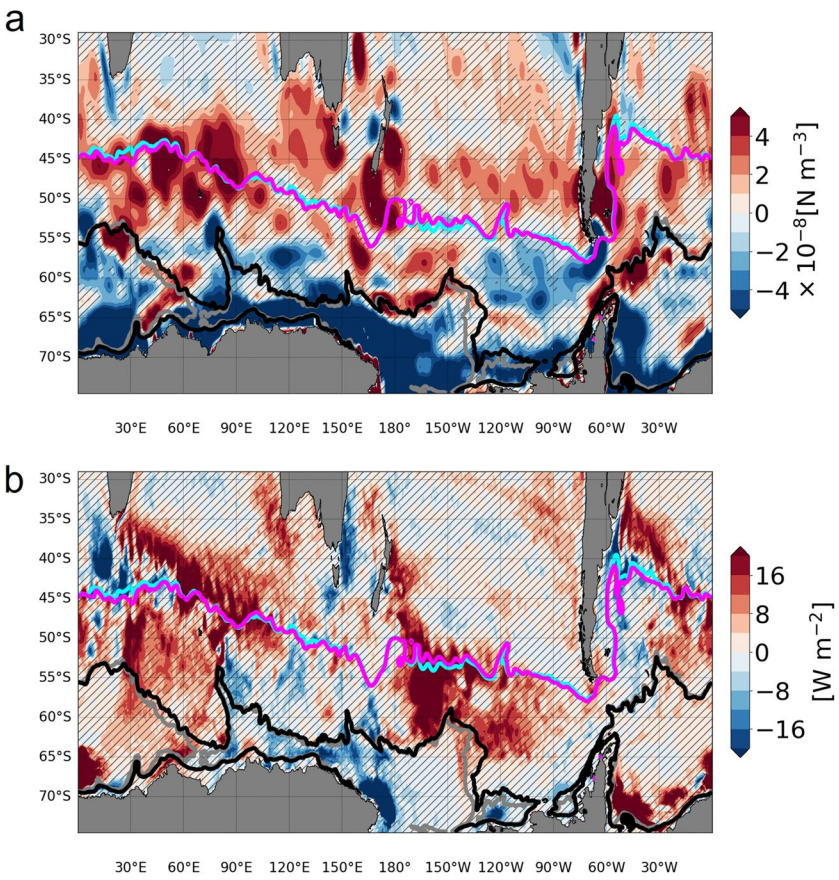

Fig. 12 Differences between SW and WW in (**a**) wind stress curl and (**b**) atmospheric heat flux. The definitions of the curves are the same as those for the sensitivity experiment (Fig. 3); however, here the curves are defined for WW and SW. Hatched regions indicate statistically nonsignificant values at a 95% confidence level in Welch's test. Welch's test is conducted for the monthly averaged time series of each period

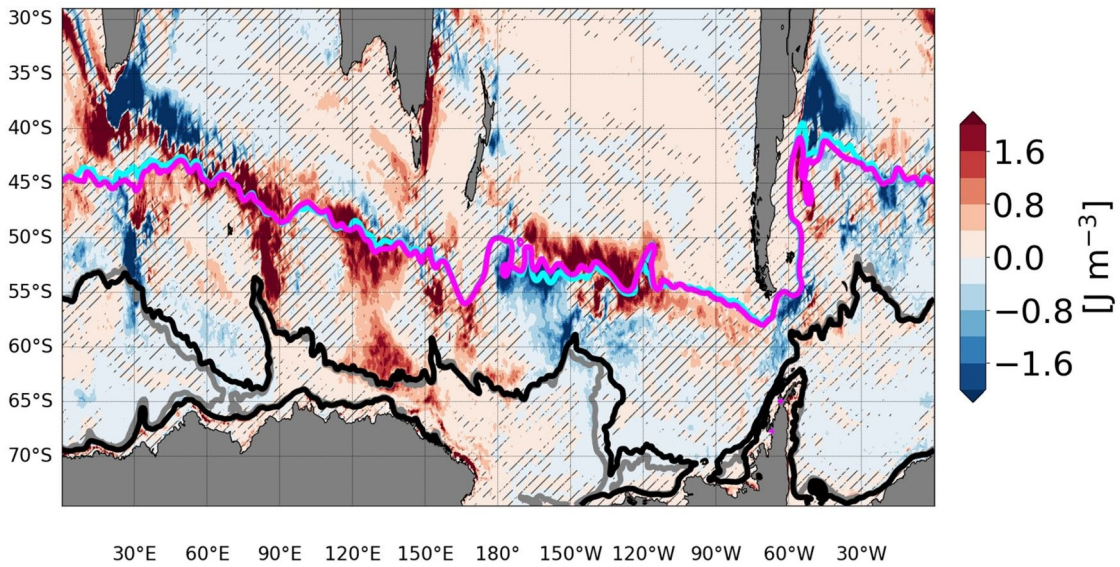

Fig. 13 EKE change from the WW to the SW period. The definitions of the curves are the same as those for the sensitivity experiment (Fig. 3); however, here the curves are defined for WW and SW. Hatched regions indicate statistically nonsignificant values at a 95% confidence level in Welch's test. Welch's test is conducted for the monthly averaged time series of each period. It is noted that the color scale is different from that of Fig. 3b because of the missing intra-monthly variabilities in the monthly data

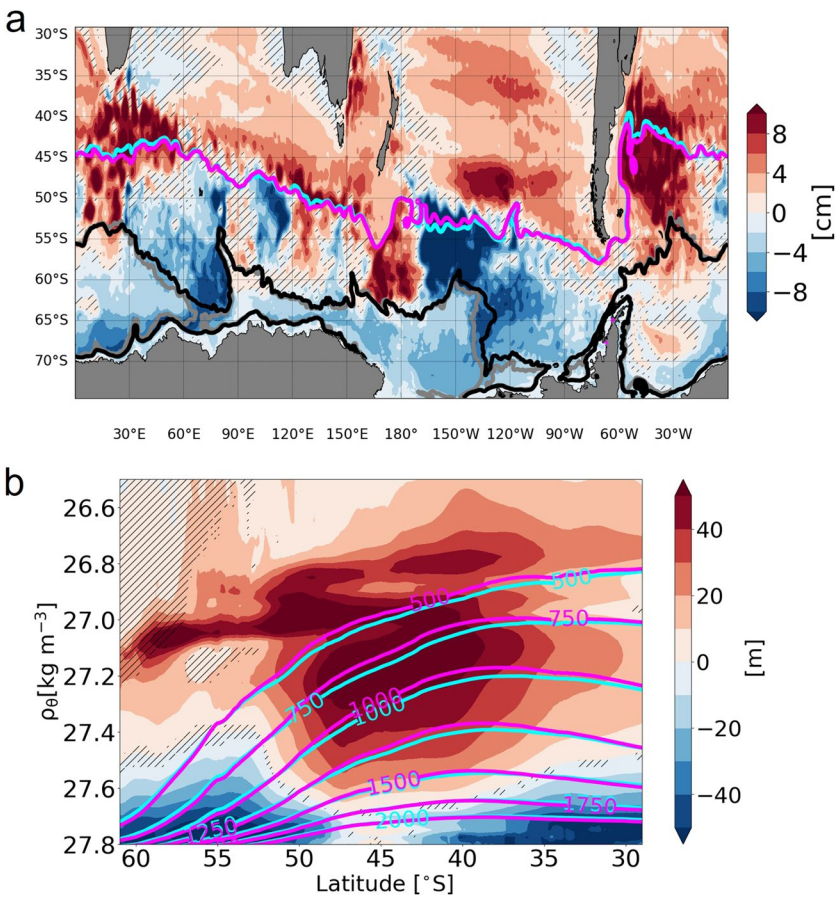

Fig. 14 **a** Sea surface height difference of the SW period from the WW period. The definitions of the curves are the same as those for the sensitivity experiment (Fig. 3); however, here the curves are defined for WW and SW. **b** Zonally averaged isopycnic depths for WW (cyan contours) and SW (magenta contours) and their changes (color shading) from WW to SW. In both panels, hatched regions indicate statistically nonsignificant values at a 95% confidence level in Welch's test. Welch's test is conducted for the monthly averaged time series of each period. It is noted that the color scales are different from those of Fig. 7

gyres in the northern half and enhance the Ekman upwelling in the southern half, which should increase isopycnal slopes across the SAF. Further, Fig. 12b presents plots of changes in surface heat flux; here, a positive value of heat flux indicates the downward heat flux. The heat flux anomalies are positive inside the ACC, which tends to reduce the isopycnal slope across the SAF. However, as shown below, the meridional density gradients increase at the main pycnocline levels, which must be due to changes in wind stress curl. The potential impacts of sea surface heat flux changes will be discussed in Section 5.

We next show the EKE changes from the WW to the SW period (Fig. 13). Although the increase is smaller than that in the sensitivity experiment, the horizontal distribution is similar. The EKE increase is significant in the region between 100°E and 140°E, the region between 120°W and 180°, and the hotspots of the Indian sector.

Differences in SSH and isopycnal surface depth between SW and WW are shown in Fig. 14. We find that the subtropical gyres are intensified in SW along the SAF (Fig. 14a), which is consistent with the results of the sensitivity analysis (Fig. 7a). In particular, the anomalies are significant in the SAF regions between 90°W and 150°W, between 90°E and 170°E, and between 30°E and 60°E.

Table 2 Same as Table 1 but for WW and SW

	WW	SW
f_0	-1.1×10^{-4} s^{-1}	—
β	1.6×10^{-11} m^{-1}s^{-1}	—
U_1	7.7 cm s^{-1}	11.0 cm s^{-1}
U_2	0.83 cm s^{-1}	1.26 cm s^{-1}
H_1	1061 m	1055 m
H_2	2939 m	2945 m
g'	0.81×10^{-2} m s^{-2}	0.83×10^{-2} m s^{-2}

The negative SSH anomalies are also prominent south of the SAF. The horizontal distribution of these changes is roughly consistent with that of the wind stress curl change (Fig. 12a). Consistent with the SSH change, the thermocline depth also changes. As in the sensitivity analysis (Fig. 7b), Fig. 14b indicates that the thermocline deepens by approximately 50 m between 40°S and 50°S, while it shoals in the ACC interior. As in the sensitivity experiment (Section 3.3), the reason for the EKE increase along the SAF (Fig. 13) is likely due to the increased baroclinicity caused by the changes in the subtropical gyre and Ekman pumping.

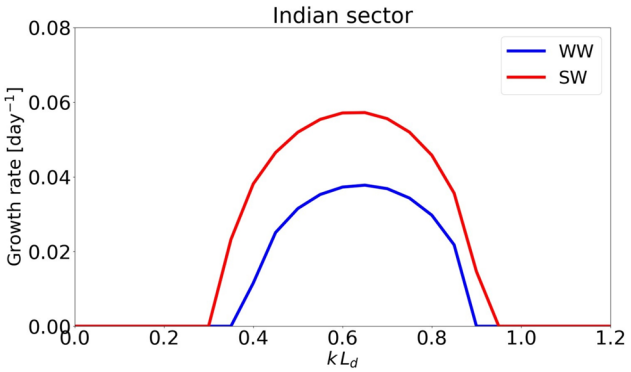

Fig. 15 Blue and red lines indicate growth rate as a function of zonal wave number normalized by the deformation radius, L_d, for WW and SW, respectively

4.2 Stability of the mean flow in the OFES hindcast

We next perform the same stability analysis as we did for the sensitivity experiment (Section 3.3) for the region 110°λ120°E, 47°λ50°S, where EKE increases significantly. Table 2 summarizes the layer thickness and the zonal velocity for each period. Similar to the sensitivity experiment, the most significant change is the increase in U_1. The growth rate is plotted in Fig. 15. The maximum growth rate of SW is 1.5 times as large as that of WW. In addition, the window of baroclinic instability is wider in the SW period than that in the WW period. These results are similar to those of the sensitivity analysis (c.f., Fig. 10), suggesting that changes in wind stress curl have led to enhanced eddy activities along the SAF since the middle of the twentieth century.

5 Summary and conclusion

In this study, we discussed the eddy responses of the ACC to intensified westerlies. We intensified wind stress between 40°S and 60°S in an OFES climatological run and compared it with the reference climatological run. The SSH anomalies of the strong wind experiment from the reference case suggest that the changes in the wind stress curl lead to the enhanced EKE of the SAF. The increased wind stress curl increases the upwelling inside the ACC and enhances the subtropical gyres north of the SAF, which deepens the thermocline north of the SAF; the opposite is the case south of the SAF. Consequently, the vertical shear of the zonal velocity increases. The linear stability analysis in the simple two-layered quasi-geostrophic framework shows that the changes in the surface velocity increase the eddy growth rate under intensified wind stress, while the changes in the stratification have a secondary role. Therefore, the eddy activity significantly increases along the SAF in addition to the well-studied increase at the eddy hotspots downstream of significant topographic features. Using the LEC, we showed that the baroclinic energy pathway dominates the responses to the wind stress changes, while the barotropic pathway is minor. Therefore, we conclude that the enhanced wind stress curl due to the increased westerlies steepens the isopycnal slope across the SAF, which enables the SAF regions to behave as "hotspots." To confirm the above scenario for a more realistic long-term trend, we divided the ~ 60-year OFES hindcast run into the first and second halves, carried out similar analyses on the two periods, and obtained very similar results.

Notably, using an idealized channel model, Youngs et al. (2017) suggested that the barotropic energy conversion is comparable with the baroclinic energy conversion under intensified westerlies; however, the OFES results suggest that the baroclinic pathway remains the dominant energy pathway. A possible reason for the difference is the horizontal shear of mean flow. In the idealized channel model of Youngs et al. (2017), the northern wall blocks all geostrophic contours. The horizontal shear should become large when the circumpolar jet traverses the geostrophic contours near the northern wall, leading to a favorable condition for barotropic instability (Yang et al. 2018).

The ACC hotspots are responsible for the cross-frontal exchanges of tracers owing to eddies (Sallée et al. 2011; Thompson and Sallée 2012). It would be an interesting future study to explore how the enhanced eddy activities affect the cross-frontal exchanges along the SAF. In addition, the eddy activities may affect the carbon cycle in the globe through the modification of the meridional overturning circulation (Marshall and Speer 2012; Tamsitt et al. 2017). Simple biogeochemical box models suggest that the ocean upwelling in the high latitude regions possibly controls atmospheric CO_2 levels (Sarmiento and Toggweiler 1984; Knox and McElroy 1984; Gnanadesikan et al. 2015).

It is noted that the results presented in this work are based on an idealized framework and therefore contain some uncertainties. In the E2 simulation, the wind stress is uniformly intensified centered at 50°S, which enhances the Ekman upwelling over the ACC region and enhances the subtropical gyres north of the SAF. On the other hand, in reality, the observed changes in wind stress curl (Fig. 11a) are not uniform over the ACC region and the wind stress anomaly is smaller than in E2 (c.f. Figs. 2a and 11b). As a result, the horizontal distribution of SSH anomalies in the hindcast is different from that in the climatological experiment, although the zonally-averaged structure of isopycnal steepening is similar. Nevertheless, the sensitivity experiment in the present study is useful to highlight and clarify processes responsible for the SAF responses to the change in the wind forcing.

In addition, the linear stability analysis based on the simple Phillips model omits several potentially important processes. While the Phillips model only represents the baroclinic instability, the meridional structure of the basic state affects baroclinic instability and introduces barotropic instability. (e.g., Killworth 1980; Moore and Peltier 1989). A two-dimensional stability analysis (e.g., Killworth 1980; Lin and Pierrehumbert 1988; Moore and Peltier 1989) would be useful to explore potential interplays between barotropic and baroclinic instabilities. We also note that the linear stability analysis is only valid for the small amplitude fluctuations (Pedlosky 1987). Once the instability mode reaches a finite amplitude, the linear assumption is no longer valid. Despite these problems, the stability analysis used here can still provide useful information to assess whether instability is more likely to occur under varying wind conditions.

Finally, we note that buoyancy flux should also be discussed in future work to capture the Southern Ocean responses to global warming. The changes in the surface heat flux tend to flatten isopycnal slopes during the analyzed period of the hindcast (Fig. 11b) but have little impact on the generation of mesoscale eddies. However, the situation may change in the future. Recent studies (Shi et al. 2020, 2021; Peng et al. 2022; Gutierrez-Villanueva et al. 2023) have pointed out that the meridional heterogeneity of global warming (Armour et al. 2016; Liu et al. 2018) strengthens the surface velocity along the SAF by the intensification of the meridional density gradient. They also suggested that the changes in the buoyancy force are more efficient for the surface velocity intensification compared to the wind stress anomalies under the quadrupled CO_2 scenario. The eddy activities along the SAF are likely to be enhanced in more efficient ways by global warming.

Appendix: Linear stability analysis of classical Phillips model

Derivation of the necessary condition for baroclinic instability

The linearized PV equations are as follows:

$$\left(\frac{\partial}{\partial t}+U_1\frac{\partial}{\partial x}\right)\left[\nabla^2\psi_1'+F_1\left(\psi_2'-\psi_1'\right)\right]+\frac{\partial\psi_1'}{\partial x}\left(\beta+F_1\Delta U\right)=0, \tag{28}$$

$$\left(\frac{\partial}{\partial t}+U_2\frac{\partial}{\partial x}\right)\left[\nabla^2\psi_2'+F_2\left(\psi_1'-\psi_2'\right)\right]+\frac{\partial\psi_2'}{\partial x}\left(\beta-F_2\Delta U\right)=0, \tag{29}$$

where $\Delta U = U_1 - U_2$ is the zonal velocity difference between the layers. Substituting Eq. (24) into Eqs. (28) and (29) gives the following simultaneous equations for A_1 and A_2:

$$\left\{\left(U_1-c\right)\left(-k^2-F_1\right)+\left[\beta+F_1\Delta U\right]\right\}A_1+\left(U_1-c\right)F_1A_2=0, \tag{30}$$

$$\left(U_2-c\right)F_2A_1+\left\{\left(U_2-c\right)\left(-k^2-F_2\right)+\left[\beta-F_2\Delta U\right]\right\}A_2=0. \tag{31}$$

The nontrivial solution exists if and only if the determinant of the simultaneous equations equals zero:

$$\begin{aligned}&\left[\left(U_1-c\right)\left(-k^2-F_1\right)+\left(\beta+F_1\Delta U\right)\right]\left[\left(U_2-c\right)\left(-k^2-F_2\right)+\left(\beta-F_2\Delta U\right)\right]\\&\quad-\left(U_1-c\right)\left(U_2-c\right)F_1F_2=0.\end{aligned} \tag{32}$$

The baroclinic instability occurs when c has an imaginary part.

Influence of meridional background flow and meridional wavenumber

In the main text, we conducted the linear stability analysis under the assumption of no meridional current and zero meridional wavenumber to describe the role of zonal velocity shear as simply as possible. In this section, we extend the stability analysis including meridional velocity and finite meridional wavenumbers to confirm the robustness of our result. Here, we used "Python Quasigeostrophic Model (pyqg)" distributed at https://pyqg.readthedocs.io/en/latest/ to conduct the linear stability analysis. The code is a pseudo-spectral model that solves a layered quasi-geostrophic equation with uniform horizontal background flow. The built-in method "stability-analysis" can conduct a linear stability analysis on the classical Philips model (see https://pyqg.readthedocs.io/en/latest/examples/linear_stability.html for details). Instead of Eq. (24), we assume a wave solution

$$\psi_j' = \mathrm{Re}\, A_j e^{i(kx+ly-\omega t)},\ j=1,2 \tag{33}$$

where k and l are the zonal and meridional wave numbers, $\omega = c\sqrt{k^2+l^2}$ is the frequency of the disturbance with the phase speed of c, Re indicates the real part of the complex number, and A_i is the complex amplitude.

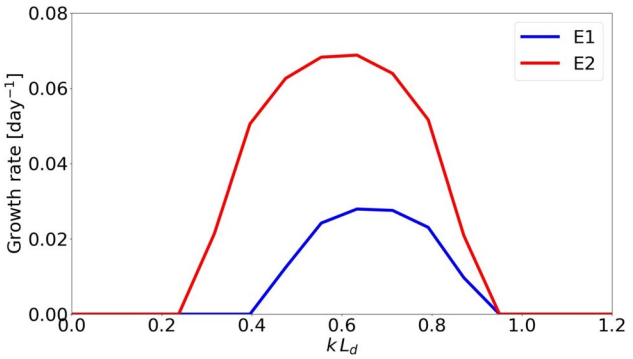

Fig. 16 Blue and red lines indicate growth rate as a function of zonal wave number normalized by the deformation radius, L_d, for E1 and E2, respectively

For the stability analysis, we determined the background meridional velocity for the Indian sector of the SAF by the same procedure as in Section 3.3. The upper- and lower-layer meridional velocities are $V_1 = -0.23\text{cm s}^{-1}$ and $V_2 = -0.17\text{cm s}^{-1}$ for E1, and $V_1 = -3.3\text{cm s}^{-1}$ and $V_2 = -0.40\text{cm s}^{-1}$ for E2. The other parameters are the same as those in Table 1. First, we calculated the growth rate with

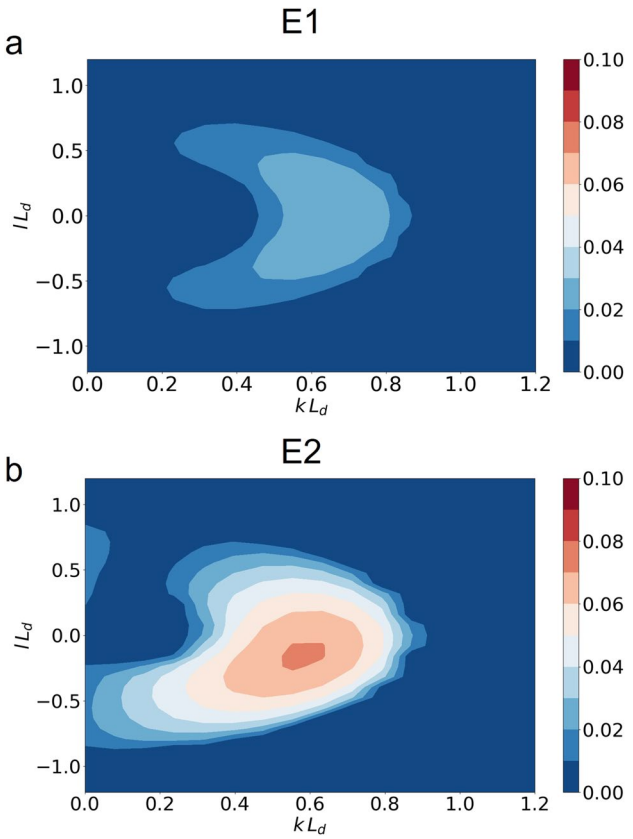

Fig. 17 The maximum growth rate for (**a**) and (**b**) E2 against zonal and meridional wavenumbers normalized by the deformation radius, L_d

$l = 0$ (Fig. 16). The amplitude and the unstable window are similar to those for E1 and E2 (Fig. 10a), although the unstable window for E1 slightly widens by the meridional flow.

In addition, we plot the maximum growth rate against the zonal and meridional wavenumbers normalized by the Rossby deformation radius (Fig. 17). In E1, the maximum growth rate is approximately symmetric for the meridional wavenumber and is largest when $lL_d \approx 0$. In E2, the growth rate is asymmetric, and the maximum growth rate is larger on the negative l side with the largest value at $lL_d \approx -0.25$. The unstable window is wider for $lL_d \approx -0.25$ than for $lL_d \approx 0$. Other than this qualitative difference, the results of our stability analysis are little affected.

Acknowledgements Takuro Matsuta was supported by Japan Society for the Promotion of Science Grant-in-Aid 22J00651 and 24K17120. Humio Mitsudera and Hideharu Sasaki were supported by Japan Society for the Promotion of Science Grant-in-Aid 19H05701.

Author contributions All authors contributed to the conceptualizations. H. S. conducted model experiments. T.M. conducted the formal analysis. T. M. and R. F. wrote the main manuscript text. T. M. prepared all figures and tables. All authors reviwed the manuscript.

Funding Takuro Matsuta was supported by Japan Society for the Promotion of Science Grant-in-Aid 22J00651 and 24K17120. Humio Mitsudera and Hideharu Sasaki were supported by Japan Society for the Promotion of Science Grant-in-Aid 19H05701. Yukio Masumoto, Ryo Furue, and Tomomichi Ogata did not receive support from any organization for the submitted work.

Data availability The data of the E1 experiment and the hindcast run is available from https://doi.org/10.17596/0002029. The data of the E2 experiment is available on request.

Declarations

Competing interests The authors declare no competing interests.

References

Abernathey R, Cessi P (2014) Topographic enhancement of Eddy efficiency in baroclinic equilibration. J Phys Oceanogr 44:2107–2126. https://doi.org/10.1175/JPO-D-14-0014.1

Aiki H, Richards KJ (2008) Energetics of the global ocean: he role of layer-thickness form drag. J Phys Oceanogr 38:1845–1869. https://doi.org/10.1175/2008JPO3820.1

Aiki H, Richards KJ, Sakuma H (2011) Maintenance of the mean kinetic energy in the global ocean by the barotropic and baroclinic energy routes: he roles of JEBAR and Ekman dynamics. Ocean Dyn 61:675–700. https://doi.org/10.1007/s10236-011-0382-y

Aiki H, Zhai X, Greatbatch RJ (2016) Energetics of the global ocean: he role of mesoscale eddies. World Sci Ser Asia-Pac Weather Clim 7:109–134. https://doi.org/10.1142/9789814696623_0004

Armour KC, Marshall J, Scott JR, Donohoe A, Newsom ER (2016) Southern Ocean warming delayed by circumpolar upwelling and equatorward transport. Nat Geosci 9:549–554. https://doi.org/10.1038/ngeo2731

Barthel A, Hogg AM, Waterman S, Keating S (2022) Baroclinic ontrol of Southern Ocean Eddy upwelling near topography. Geophys Res Lett 49:e2021GL097491. https://doi.org/10.1029/2021gl097491

Barthel A, McC A, Hogg SW, Keating S (2017) Jet-topography interactions affect energy pathways to the deep Southern Ocean. J Phys Oceanogr 47:1799–1816. https://doi.org/10.1175/JPO-D-16-0220.1

Bischoff T, Thompson AF (2014) Configuration of a Southern Ocean storm track. J Phys Oceanogr 44:3072–3078. https://doi.org/10.1175/JPO-D-14-0062.1

Bishop SP, Gent PR, Bryan FO, Thompson AF, Long MC, Abernathey R (2016) Southern ocean overturning compensation in an eddy-resolving climate simulation. J Phys Oceanogr 46:1575–1592. https://doi.org/10.1175/JPO-D-15-0177.1

Böning CW, Dispert A, Visbeck M, Rintoul SR, Schwarzkopf FU (2008) The response of the Antarctic Circumpolar Current to recent climate change. Nat Geosci 1:864–869. https://doi.org/10.1038/ngeo362

Chapman CC, Hogg AMC, Kiss AE, Rintoul SR (2015) The dynamics of Southern Ocean storm tracks. J Phys Oceanogr 45:884–903. https://doi.org/10.1175/JPO-D-14-0075.1

Chen R, Flierl GR, Wunsch C (2014) A description of local and nonlocal eddy-mean flow interaction in a global eddy-permitting state estimate. J Phys Oceanogr 44:2336–2352. https://doi.org/10.1175/JPO-D-14-0009.1

Chen R, Thompson AF, Flierl GR (2016) Time-dependent eddy-mean energy diagrams and their application to the ocean. J Phys Oceanogr 46:2827–2850. https://doi.org/10.1175/JPO-D-16-0012.1

Donohue KA, Tracey KL, Watts DR, Chidichimo MP, Chereskin TK (2016) Mean antarctic circumpolar current transport measured in Drake Passage. Geophys Res Lett 43:11760–11767. https://doi.org/10.1002/2016GL070319

Dufour CO, Sommer LL, Zika JD, Gehlen M, Orr JC, Mathiot P, Barnier B (2012) Standing and transient eddies in the response of the Southern Ocean meridional overturning to the Southern annular mode. J Clim 25:6958–6974. https://doi.org/10.1175/JCLI-D-11-00309.1

Farneti R, Delworth TL, Rosati AJ, Griffies SM, Zeng F (2010) The role of mesoscale eddies in the rectification of the Southern ocean response to climate change. J Phys Oceanogr 40:1539–1557. https://doi.org/10.1175/2010JPO4353.1

Fogt RL, Marshall GJ (2020) The Southern annular mode: Variability, trends, and climate impacts across the Southern Hemisphere. Wiley Interdiscip Rev Clim Change 11:e652. https://doi.org/10.1002/wcc.652

Foppert A (2019) Observed storm track dynamics in Drake Passage. J Phys Oceanogr 49:867–884. https://doi.org/10.1175/JPO-D-18-0150.1

Foppert A, Donohue KA, Watts DR, Tracey KL (2017) Eddy heat flux across the Antarctic circumpolar current estimated from sea surface height standard deviation. J Geophys Res Oceans 122:6947–6964. https://doi.org/10.1002/2017JC012837

Frenger I, Münnich M, Gruber N, Knutti R (2015) Southern Ocean eddy phenomenology. J Geophys Res Oceans 120:7413–7449. https://doi.org/10.1002/2015JC011047

Fyfe JC, Saenko OA (2005) Human-induced change in the Antarctic Circumpolar Current. J Clim 18:3068–3073. https://doi.org/10.1175/JCLI3447.1

Fyfe JC, Saenko OA (2006) Simulated changes in the extratropical Southern Hemisphere winds and currents. Geophys Res Lett 33:1–4. https://doi.org/10.1029/2005GL025332

Gnanadesikan A, Hallberg RW (2000) On the relationship of the circumpolar current to Southern Hemisphere winds in coarse-resolution ocean models. J Phys Oceanogr 30:2013–2034. https://doi.org/10.1175/1520-0485(2000)030<2013:OTROTC>2.0.CO;2

Gnanadesikan A, Pradal M, Abernathey R (2015) Isopycnal mixing by mesoscale eddies significantly impacts oceanic anthropogenic carbon uptake. Geophys Res Lett 42:4249–4255. https://doi.org/10.1002/2015GL064100

Gong D, Wang S (1999) Definition of Antarctic oscillation index. Geophys Res Lett 26:459–462. https://doi.org/10.1029/1999GL900003

Gutierrez-Villanueva MO, Chereskin TK, Sprintall J (2023) Compensating transport trends in the Drake Passage frontal regions yield no acceleration in net transport. Nat Commun 14:7792. https://doi.org/10.1038/s41467-023-43499-2

Hallberg R, Gnanadesikan A (2006) The Role of Eddies in determining the structure and response of the wind-driven Southern Hemisphere overturning: results from the modeling Eddies in the Southern Ocean (MESO) project. J Phys Oceanogr 36:2232–2252. https://doi.org/10.1175/JPO2980.1

Hogg AMC, Penduff T, Close SE, Dewar WK, Constantinou NC, Martínez-Moreno J (2022) Circumpolar variations in the chaotic nature of Southern Ocean Eddy Dynamics. J Geophys Res Oceans 127. https://doi.org/10.1029/2022JC018440

Hughes CW (2005) Nonlinear vorticity balance of the Antarctic Circumpolar Current. J Geophys Res Oceans 110:1–11. https://doi.org/10.1029/2004JC002753

Jouanno J, Capet X (2020) Connecting flow-topography interactions, vorticity balance, baroclinic instability and transport in the Southern Ocean: The case of an idealized storm track. Ocean Sci 16:1207–1223. https://doi.org/10.5194/os-16-1207-2020

Kalnay E, Coauthors (1996) The NCEP/NCAR 40-year reanalysis project. Bull Am Meteorol Soc 77:437–471. https://doi.org/10.1175/1520-0477(1996)077%3c0437:TNYRP%3e2.0.CO;2

Karsten R, Jones H, Marshall J (2002) The role of eddy transfer in setting the stratification and transport of a circumpolar current. J Phys Oceanogr 32:39–54. https://doi.org/10.1175/1520-0485(2002)032<0039:TROETI>2.0.CO;2

Katsumata K (2017) Eddies observed by Argo floats. Part II: form stress and streamline length in the Southern Ocean. J Phys Oceanogr 47:2237–2250. https://doi.org/10.1175/JPO-D-17-0072.1

Killworth PD (1980) Barotropic and baroclinic instability in rotating stratified fluids. Dyn Atmos Oceans 4:143–184. https://doi.org/10.1016/0377-0265(80)90013-5

Kim YS, Orsi AH (2014) On the variability of antarctic circumpolar current frontsInferred from 1992–2011 altimetry*.

J Phys Oceanogr 44:3054–3071. https://doi.org/10.1175/JPO-D-13-0217.1
Knox F, McElroy MB (1984) Changes in atmospheric CO2: influence of the marine biota at high latitude. J Geophys Res 89:4629–4637. https://doi.org/10.1029/JD089iD03p04629
Koenig Z, Provost C, Ferrari R, Sennéchael N, Rio M (2014) Volume transport of the Antarctic Circumpolar Current: roduction and validation of a 20 year long time series obtained from in situ and satellite observations. J Geophys Res Oceans 119:5407–5433. https://doi.org/10.1002/2014JC009966
Krupitsky A, Cane MA (1994) On topographic pressure drag in a zonal channel. J Mar Res 52:1–23. https://doi.org/10.1357/0022240943076740
LaCasce JH, Isachsen PE (2010) The linear models of the ACC. Prog Oceanogr 84:139–157. https://doi.org/10.1016/j.pocean.2009.11.002
Lin S-J, Pierrehumbert RT (1988) Does Ekman friction suppress baroclinic instability? J Atmos Sci 45:2920–2933. https://doi.org/10.1175/1520-0469(1988)045<2920:DEFSBI>2.0.CO;2
Liu W, Lu J, Xie S-P, Fedorov A (2018) Southern Ocean heat uptake, redistribution, and storage in a warming climate: the role of meridional overturning circulation. J Clim 31:4727–4743. https://doi.org/10.1175/JCLI-D-17-0761.1
Lorenz EN (1955) Available potential energy and the maintenance of the general circulation. Tellus 7:157–167. https://doi.org/10.1111/j.2153-3490.1955.tb01148.x
Marshall GJ (2003) Trends in the Southern Annular Mode from observations and reanalyses. J Clim 16:4134–4143. https://doi.org/10.1175/1520-0442(2003)016<4134:TITSAM>2.0.CO;2
Marshall J, Speer K (2012) Closure of the meridional overturning circulation through Southern Ocean upwelling. Nat Geosci 5:171–180. https://doi.org/10.1038/ngeo1391
Mason E, Pascual A, Gaube P, Ruiz S, Pelegrí JL, Delepoulle A (2017) Subregional characterization of mesoscale eddies across the Brazil-Malvinas Confluence. J Geophys Res Oceans 122:3329–3357. https://doi.org/10.1002/2016JC012611
Masumoto Y, Sasaki H, Kagimoto T, Komori N, Ishida A, Sasai Y, Miyama T, Motoi T, Mitsudera H, Takahashi K, Sakuma H, Yamagata T (2004) A fifty-year eddy-resolving simulation of the world ocean: preliminary outcomes of OFES (OGCM for the Earth Simulator). J Earth Simul 1:35–56. https://doi.org/10.32131/jes.1.35
Matsuta T (2022) Spatial heterogeneity of eddy-mean flow interactions in the Antarctic Circumpolar Current. PhD Thesis, The University of Tokyo, Tokyo
Matsuta T, Masumoto Y (2021) Modified view of energy budget diagram and its application to the Kuroshio Extension Region. J Phys Oceanogr 51:1163–1175. https://doi.org/10.1175/JPO-D-20-0124.1
Matsuta T, Masumoto Y (2023) Energetics of the Antarctic Circumpolar Current. Part I: the lorenz energy cycle and the vertical energy redistribution. J Phys Oceanogr 53:1467–1484. https://doi.org/10.1175/jpo-d-22-0133.1
Moore GWK, Peltier WR (1989) Nonseparable baroclinic instability. Part I: Quasi-geostroPhic Dynamics. J Atmos Sci 46:57–78. https://doi.org/10.1175/1520-0469(1989)046<0057:NBIPIQ>2.0.CO;2
Murakami S (2011) Atmospheric local energetics and energy interactions between mean and eddy fields. Part I: Theory. J Atmos Sci 68:760–768. https://doi.org/10.1175/2010JAS3664.1
Nadeau LP, Ferrari R (2015) The role of closed gyres in setting the zonal transport of the antarctic circumpolar current. J Phys Oceanogr 45:1491–1509. https://doi.org/10.1175/JPO-D-14-0173.1
Pedlosky J (1987) Geophysical fluid dynamics. Springer, New York
Peng Q, Xie S-P, Wang D, Huang RX, Chen G, Shu Y, Shi J-R, Liu W (2022) Surface warming–induced global acceleration of upper ocean currents. Sci Adv 8:8394. https://doi.org/10.1126/sciadv.abj8394
Rintoul SR (2018) The global influence of localized dynamics in the Southern Ocean. Nature 558:209–218. https://doi.org/10.1038/s41586-018-0182-3
Roquet F, Wunsch C, Madec G (2011) On the patterns of wind-power input to the ocean circulation. J Phys Oceanogr 41:2328–2342. https://doi.org/10.1175/JPO-D-11-024.1
Saenko OA, Fyfe JC, England MH (2005) On the response of the oceanic wind-driven circulation to atmospheric CO2 increase. Clim Dyn 25:415–426. https://doi.org/10.1007/s00382-005-0032-5
Sallée JB, Speer K, Rintoul SR (2011) Mean-flow and topographic control on surface eddy-mixing in the Southern Ocean. J Mar Res 69:753–777. https://doi.org/10.1357/002224011799849408
Sarmiento JL, Toggweiler JR (1984) A new model for the role of the oceans in determining atmospheric P CO2. Nature 308:621–624. https://doi.org/10.1038/308621a0
Sasaki H, Sasaki H, Sasai Y, Kawahara S, Furuichi M, Araki F, Ishida A et al (2004) A series of eddy-resolving ocean simulations in the world ocean–OFES (OGCM for the Earth Simulator) project. In: Ocean '04–MTS/IEEE Techno-Ocean '04: Bridges across the Oceans–Conference Proceedings, vol 3, pp 1535–1541. https://doi.org/10.1109/oceans.2004.1406350
Sasaki H, Nonaka M, Masumoto Y, Sasai Y, Uehara H, Sakuma H (2008) An Eddy-Resolving hindcast simulation of the Quasi-global Ocean from 1950 to 2003 on the earth simulator. In: High resolution numerical modelling of the atmosphere and ocean. Springer, New York, pp 157–185. https://doi.org/10.1007/978-0-387-49791-4_10
Scotti A, White B (2014) Diagnosing mixing in stratified turbulent flows with a locally defined available potential energy. J Fluid Mech 740:114–135. https://doi.org/10.1017/jfm.2013.643
Shi JR, Talley LD, Xie SP, Peng Q, Liu W (2021) Ocean warming and accelerating Southern Ocean zonal flow. Nat Clim Chang 11:1090. https://doi.org/10.1038/s41558-021-01212-5
Shi J-R, Talley LD, Xie S-P, Liu W, Gille ST (2020) Effects of buoyancy and wind forcing on Southern Ocean climate change. J Clim 33:10003–10020. https://doi.org/10.1175/JCLI-D-19-0877.1
Spence P, Fyfe JC, Montenegro A, Weaver AJ (2010) Southern ocean response to strengthening winds in an eddy-permitting global climate model. J Clim 23:5332–5343. https://doi.org/10.1175/2010JCLI3098.1
Stewart AL, Hogg AMC (2017) Reshaping the antarctic circumpolar current via antarctic bottom water export. J Phys Oceanogr 47:2577–2601. https://doi.org/10.1175/JPO-D-17-0007.1
Stewart AL, Neumann NK, Solodoch A (2023) "Eddy" saturation of the antarctic circumpolar current by standing waves. J Phys Oceanogr 53:1161–1181. https://doi.org/10.1175/jpo-d-22-0154.1
Straub DN (1993) On the transport and angular momentum balance of channel models of the Antarctic Circumpolar Current. J Phys Oceanogr 23:776–782. https://doi.org/10.1175/1520-0485(1993)023<0776:OTTAAM>2.0.CO;2
Talley L (2013) Closure of the global overturning circulation through the Indian, Pacific, and Southern Oceans: schematics and transports. Oceanography 26:80–97. https://doi.org/10.5670/oceanog.2013.07
Tamsitt V, Coauthors (2017) Spiraling pathways of global deep waters to the surface of the Southern Ocean. Nat Commun 8:1–10. https://doi.org/10.1038/s41467-017-00197-0
Thompson AF, Naveira Garabato AC (2014) Equilibration of the Antarctic Circumpolar Current by standing meanders. J Phys Oceanogr 44:1811–1828. https://doi.org/10.1175/JPO-D-13-0163.1
Thompson AF, Sallée JB (2012) Jets and Topography: jet transitions and the impact on transport in the Antarctic Circumpolar Current. J Phys Oceanogr 42:956–972. https://doi.org/10.1175/JPO-D-11-0135.1

Treguier AM, Le Sommer J, Molines JM, de Cuevas B (2010) Response of the southern ocean to the southern annular mode: Interannual variability and multidecadal trend. J Phys Oceanogr 40:1659–1668. https://doi.org/10.1175/2010JPO4364.1

Vallis GK (2017) Atmospheric and oceanic fluid dynamics. Cambridge University Press, Cambridge. https://doi.org/10.1017/9781107588417

Wang L, Huang RX (1995) A linear homogeneous model of wind-driven circulation in a β-Plane Channel. J Phys Oceanogr 25:587–603. https://doi.org/10.1175/1520-0485(1995)025<0587:ALHMOW>2.0.CO;2

Wu Y, Wang Z, Liu C (2017) On the response of the Lorenz energy cycle for the Southern Ocean to intensified westerlies. J Geophys Res Oceans 122:2465–2493. https://doi.org/10.1002/2016JC012539

Yang H, Qiu B, Chang P, Wu L, Wang S, Chen Z, Yang Y (2018) Decadal variability of Eddy characteristics and energetics in the kuroshio extension: unstable versus stable states. J Geophys Res Oceans 123:6653–6669. https://doi.org/10.1029/2018JC014081

Youngs MK, Thompson AF, Lazar A, Richards KJ (2017) ACC meanders, energy transfer, and mixed barotropic-baroclinic instability. J Phys Oceanogr 47:1291–1305. https://doi.org/10.1175/JPO-D-16-0160.1

Youngs MK, Flierl GR, Ferrari R (2019) Role of residual overturning for the sensitivity of southern ocean isopycnal slopes to changes in wind forcing. J Phys Oceanogr 49:2867–2881. https://doi.org/10.1175/JPO-D-19-0072.1

Yung CK, Morrison AK, Hogg AMC (2022) Topographic hotspots of Southern Ocean Eddy Upwelling. Front Mar Sci 9. https://doi.org/10.3389/fmars.2022.855785

Zemskova VE, White BL, Scotti A (2015) Available potential energy and the general circulation: Partitioning wind, buoyancy forcing, and diapycnal mixing. J Phys Oceanogr 45:1510–1531. https://doi.org/10.1175/JPO-D-14-0043.1

Zhang X, Nikurashin M, Peña-Molino B, Rintoul SR, Doddridge E (2023) A theory of standing meanders of the Antarctic Circumpolar Current and their response to wind. J Phys Oceanogr 53:235–251. https://doi.org/10.1175/JPO-D-22-0086.1

Zhu Y, Qiu B, Lin X, Wang F (2018) Interannual Eddy kinetic energy modulations in the agulhas return current. J Geophys Res Oceans 123:6449–6462. https://doi.org/10.1029/2018JC014333

Zika JD, Coauthors (2013) Vertical eddy fluxes in the Southern Ocean. J Phys Oceanogr 43:941–955. https://doi.org/10.1175/JPO-D-12-0178.1